# Supplementary Information

# Heterogeneous interface catalysts with electron local exchange towards highly selective oxidation of biomass platform compounds

**Zhen Ren,[1] Yusen Yang,*[1] Si Wang,[1] Yiming Niu,[2] Lei Wang,[1] Jun Yu,[1] Yingjie Song,[1] Xin Zhang,[1] Bingsen Zhang,[2] and Min Wei*[1]**

[1] State Key Laboratory of Chemical Resource Engineering, Beijing Advanced Innovation Center for Soft Matter Science and Engineering, Beijing University of Chemical Technology, Beijing 100029, P. R. China

[2] Shenyang National Laboratory for Materials Science, Institute of Metal Research, Chinese Academy of Sciences, Shenyang 110016, P. R. China

**Author Information**

* Corresponding authors. Tel.: +86-10-64412131; Fax: +86-10-64425385.

E-mail addresses: yangyusen@mail.buct.edu.cn (Y. Yang); weimin@mail.buct.edu.cn (M. Wei).

## Supplementary methods

**Charaterization details.** X-ray photoelectron spectra (XPS) were obtained by using an apparatus (Thermo VG Escalab 250) with Al Kα irradiation monochromatic source. Chemical state and the corresponding surface element composition of all the samples were determined by XPS Peak 4.1 program. The charge calibration was applied by setting the main C 1*s* peak at 284.8 eV. $H_2$-TPR and $O_2$-TPD was carried out in a quartz tube on an Automated Catalyst Characterization System (AutoChem 2920). For the measurements of $H_2$-TPR, the temperature was gradually raised from 50 to 700 °C at a heating rate of 5 °C $min^{-1}$, accompanied with flowing a mixed gas of $H_2$ and Ar (1:9, v/v). In the case of $O_2$-TPD, 100 mg of the sample was treated in the reactor *via* flowing a mixed gas of $O_2$ and He (1:9, v/v) at 200 °C. Subsequently, He was purged into the reactor for 60 min and then cooled down to 50 °C for the desorption of $O_2$. Finally, the sample was heated from 50 to 700 °C at a rate of 10 °C·$min^{-1}$ along with the collection of TCD signals.

***In situ* FT-IR measurements.** FT-IR measurements were carried out on a spectrometer (VERTEX 70). The window of the reaction chamber was $CaF_2$, and the reaction temperature was controlled by thermocouples. The sample (30 mg) was pressed into a round flake without carrier and installed into the reaction chamber, followed by pretreatment at 200 °C in a pure He flow for 1 h and cooled down to room temperature in He. For the adsorption of CO, IR signals were collected in a 1% CO/He flow. In order to investigate the redox property of CoMn-MOCs, FT-IR measurements of $CH_3OH$ adsorption were carried out. $CH_3OH$ was introduced into the reactor for 15 min. Subsequently, He was purged to remove the physically adsorbed molecule followed by collection of IR signals. *In situ* FT-IR measurements of HMF, DFF and FFCA adsorption and

surface reaction were performed using a transmission reactor. The sample was pretreated at 200 °C in a 10% $O_2$/He flow for 1 h and cooled down to room temperature in He. The reaction chamber was vacuumed and then the substrate was introduced. Infrared signals *vs* the reference baseline were collected. Subsequently, He was purged to remove the physically adsorbed molecule followed by collection of IR signals. Finally, the spectra during the oxidation reaction process were collected per 30 s after the introduction of $H_2O$ and 10% $O_2$/He (flow rate: 30 mL $min^{-1}$).

**Reaction kinetic studies on HMF oxidation over CoMn-MOCs catalysts.** A kinetic model was built to study the catalytic oxidation reaction of HMF and determine the rate constants of each step, according to the reported method[1]. The oxidation from HMF to HMFCA was confirmed as a first-order reaction with respect to HMF by using the differential method. The equations 1-4 describe the rate constants for each species consumed and formed in HMF oxidation reaction. The $C_{HMF}$, $C_{HMFCA}$, $C_{FFCA}$ and $C_{FDCA}$ are the concentrations of relevant reactants and products; $k_{HMF}$ and $k_{FFCA}$ are the rate constants of aldehyde groups oxidation; $k_{HMFCA}$ represents the rate constant of alcohol group oxidation.

$$\frac{dC_{HMF}}{dt} = -k_{HMF}C_{HMF} \quad (1)$$

$$\frac{dC_{HMFCA}}{dt} = k_{HMF}C_{HMF} - k_{HMFCA}C_{HMFCA} \quad (2)$$

$$\frac{dC_{FFCA}}{dt} = k_{HMFCA}C_{HMFCA} - k_{FFCA}C_{FFCA} \quad (3)$$

$$\frac{dC_{FDCA}}{dt} = k_{FFCA}C_{FFCA} \quad (4)$$

To estimate the kinetic parameters of different oxidation steps, the least-squares fitting algorithm of origin *lsqcurvefit* was used, and the following assumptions have been made:

(1) The temperature is regulated and assumed to be stable at 120 ℃ throughout the reaction.

(2) The concentrations and properties of active sites on the catalyst surface remain constant during the catalytic reaction.

(3) The reaction system is considered as a homogeneous solution.

(4) All dehydrogenation reactions are irreversible.

(5) The oxygen concentration is sufficient and invariable in the liquid phase.

**Computational details.** DFT calculations were performed through the Vienna ab initio simulation package (VASP, version 5.4) using the periodic supercell approach[2]. The projector augmented wave method (PAW) was used for electron-ion interactions[3]. Electronic structures of bulk were calculated using the Perdew-Burke-Ernzerhof (PBE)[4] form of the generalized gradient approximation expanded in a plane wave basis, and the Grimme's DFT-D3 was added to consider the effect of van der Waals interaction for surface reaction. Spin polarization was involved in all calculations. All DFT calculations were performed with a cutoff energy of 400 eV and a 3 × 3 × 1 grid generated by Monkhorst-Pack method was set to reach convergence[5]. The convergence criteria for the electronic self-consistent iteration and force were set to $10^{-4}$ eV and 0.05 eV $Å^{-1}$, respectively. The climbing image general nudged elastic band (CI-NEB) method was used to locate the transition states (TSs)[6]. Vibrational frequency analysis was performed to verify only one imaginary frequency in each transition state.

The adsorption energy ($E_{ads}$), activation energy ($E_a$) and reaction energy ($\Delta E$) were calculated based on the following three equations:

$$E_{ads} = E_{A/M} - E_A - E_M \quad (5)$$

$$E_a = E_{TS} - E_{IS} \quad (6)$$

$$\Delta E = E_{FS} - E_{IS} \quad (7)$$

where $E_A$, $E_M$, $E_{A/M}$, $E_{IS}$, $E_{TS}$, $E_{FS}$ represent the calculated energies of adsorbate, substrate, adsorption system, initial state (IS), transition state (TS) and final state (FS), respectively.

According to the results of XRD results, the (311) facet of $Co_3O_4$ was used as the initial computational mode. The $Co_3O_4/Co_2MnO_4$ interfacial sites in CoMn-MOCs-500 were constructed by replacing the four octahedral-coordinated Co atoms in $Co_3O_4$ phase with Mn. The $Co_2MnO_4$ phase with Co: Mn=2:1 was constructed by replacing seven octahedral-coordinated Co atoms with Mn atoms in $Co_3O_4$ according to the principle of maximum distribution. In each of the three models, a vacuum space of 18 Å was added in the *z* direction to minimize the interactions between adjacent slabs. Periodic boundary conditions were used for all reaction models.

## Supplementary figures

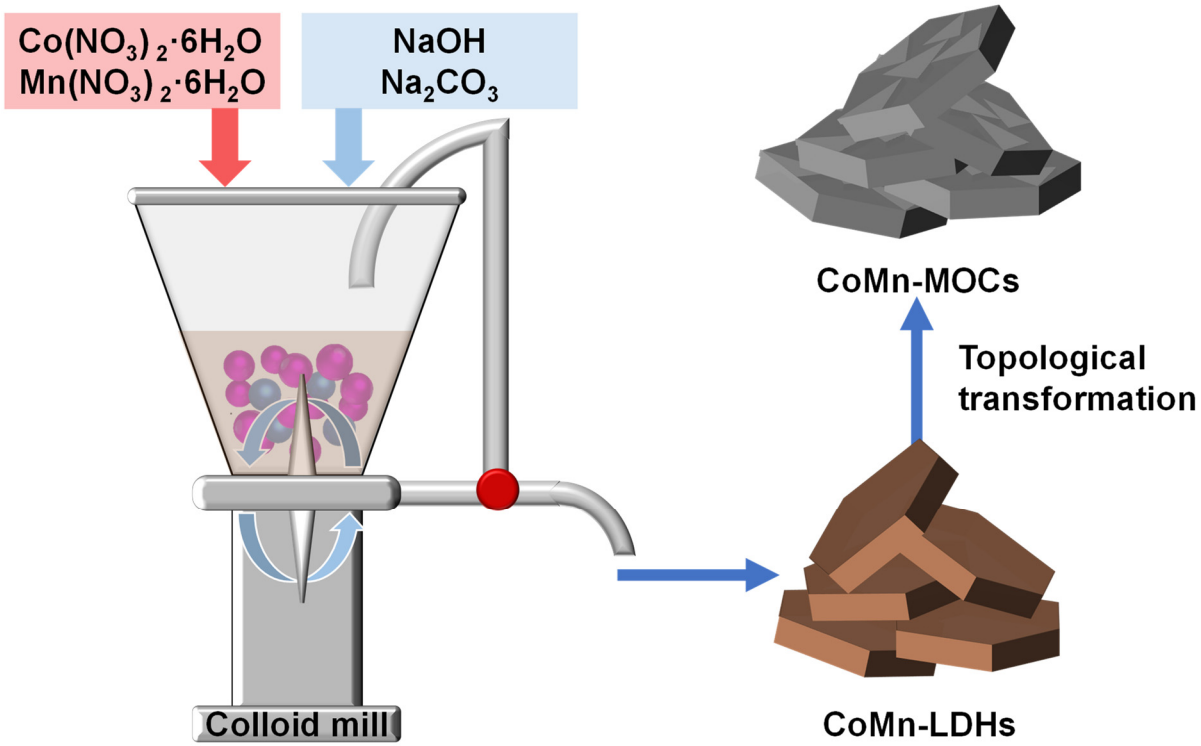


**Supplementary Figure 1 Preparation process of CoMn-MOCs.** Schematic representation for the preparation of CoMn-MOCs *via* the separate nucleation and aging steps (SNAS)[7] method followed by calcination process.

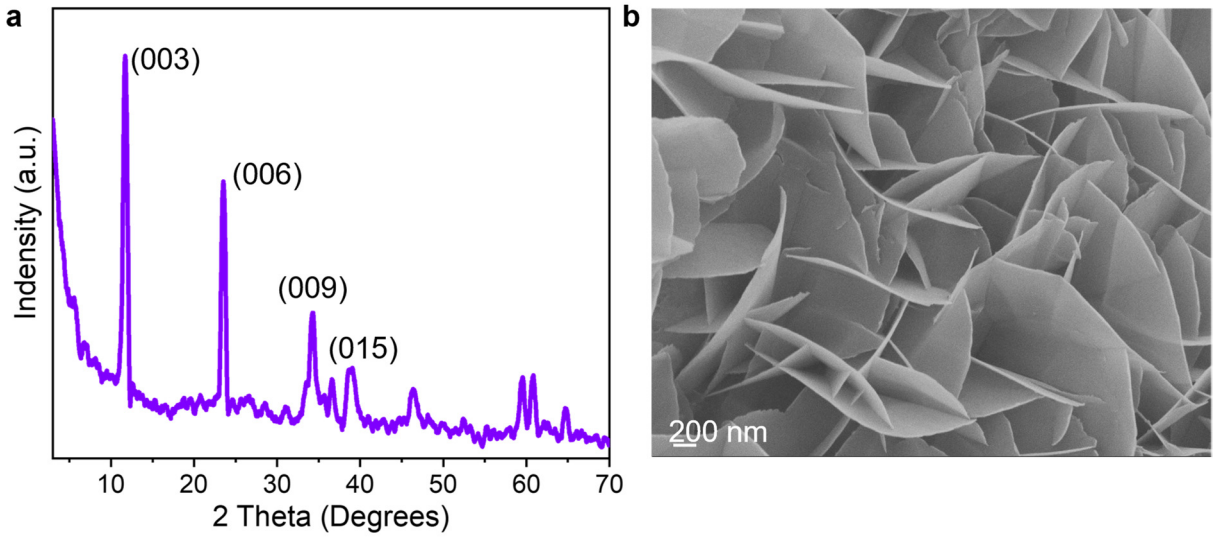


**Supplementary Figure 2 Structure characterization of CoMn-LDHs. a** XRD pattern and **b** SEM image of the CoMn-LDHs precursor.

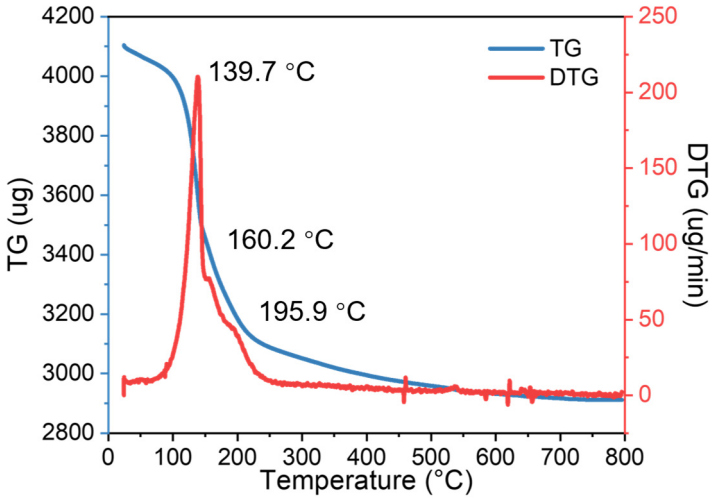


**Supplementary Figure 3 Thermal decomposition of CoMn-LDHs sample.** TG (blue line) and DTG (red line) curves of the CoMn-LDHs sample.

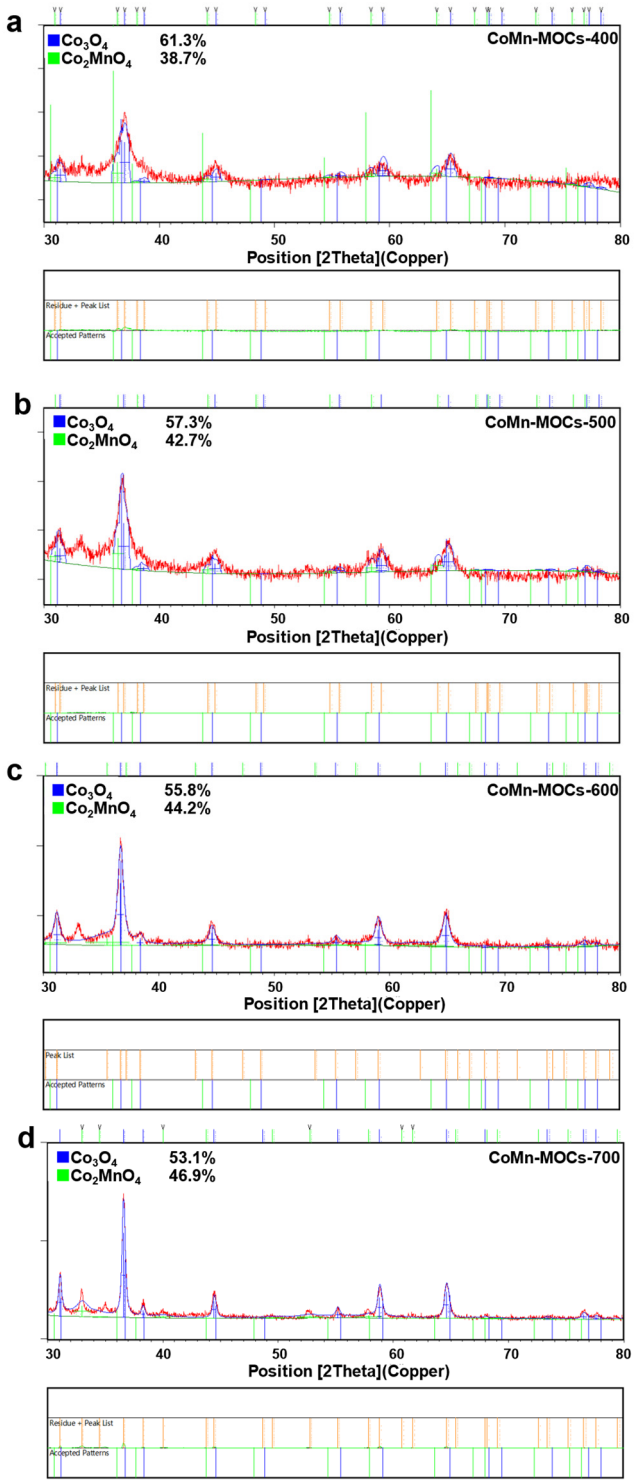


**Supplementary Figure 4 Refinement structure of CoMn-MOCs samples.** Experimental and calculated XRD patterns for **a** CoMn-MOCs-400**, b** CoMn-MOCs-500**, c** CoMn-MOCs-600 and **d** CoMn-MOCs-700 samples. The calculated patterns were obtained by the Rietveld structure refinement for the spinel structure.

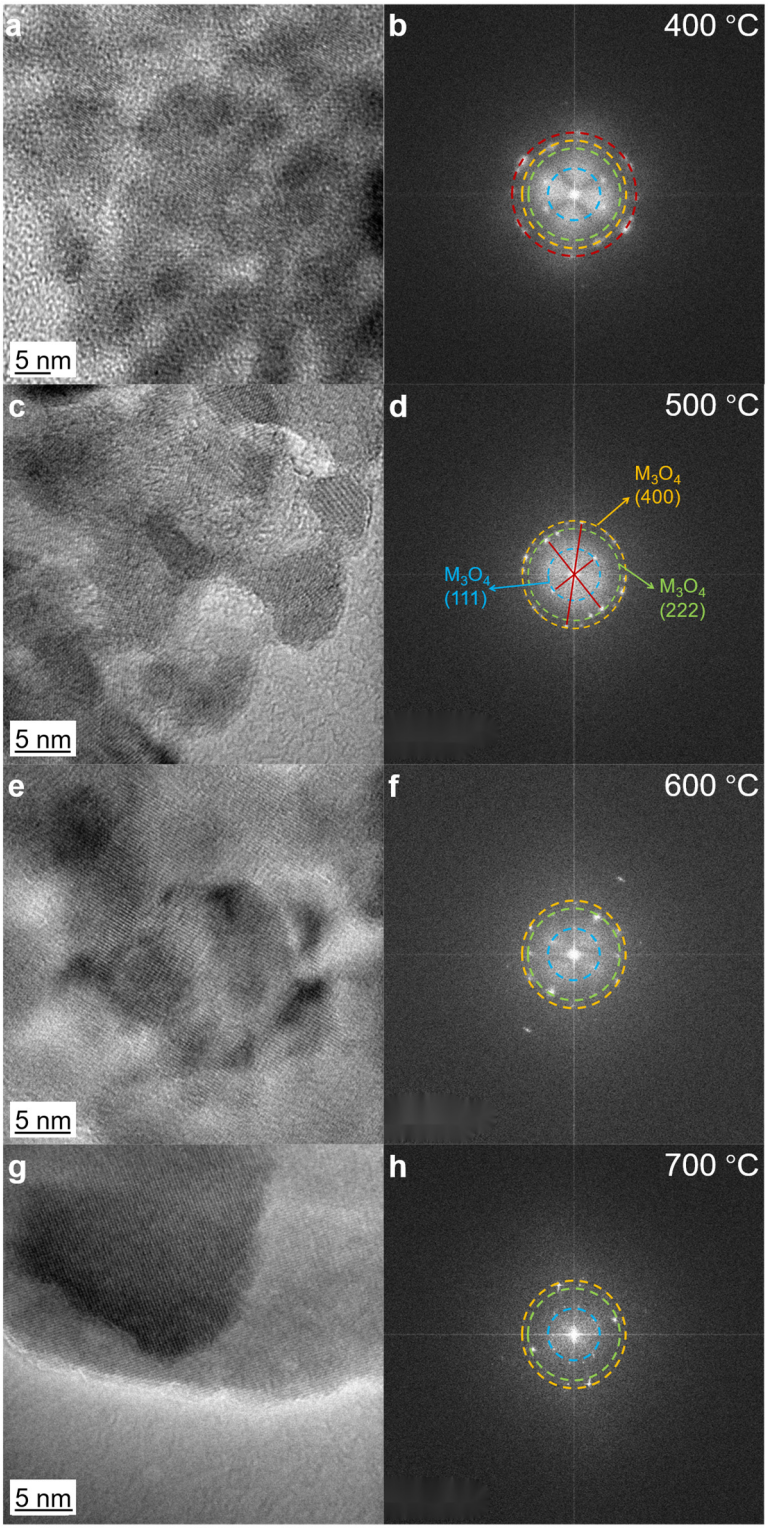


**Supplementary Figure 5 Morphology characterizations of CoMn-MOCs samples.** TEM images and corresponding FFT images of **a, b** CoMn-MOCs-400, **c, d** CoMn-MOCs-500, **e, f** CoMn-MOCs-600 and **g, h** CoMn-MOCs-700 samples, respectively.

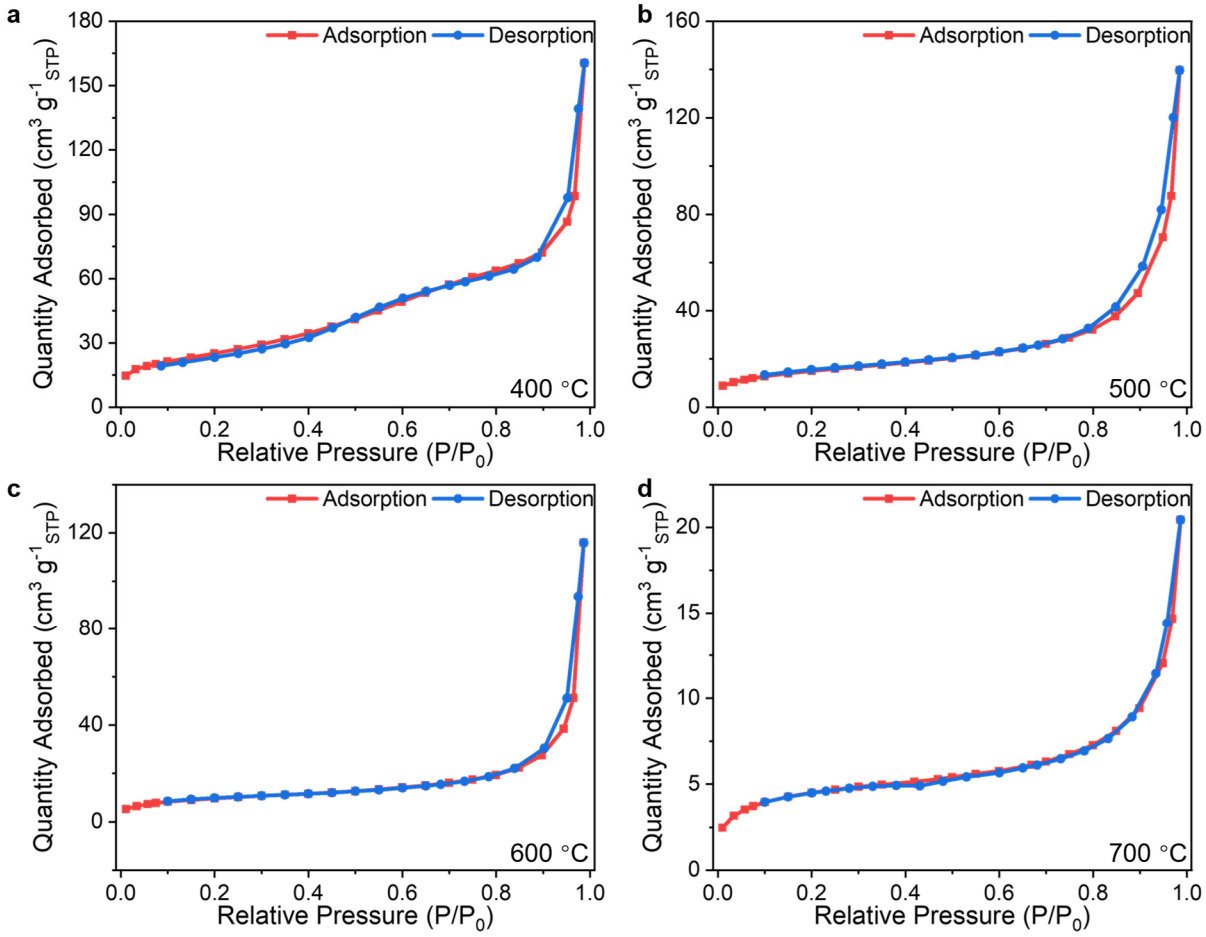


**Supplementary Figure 6 $N_2$ adsorption-desorption isotherms of CoMn-MOCs samples.** $N_2$ adsorptions-desorption isotherms of **a** CoMn-MOCs-400, **b** CoMn-MOCs-500, **c** CoMn-MOCs-600 and **d** CoMn-MOCs-700 samples, respectively.

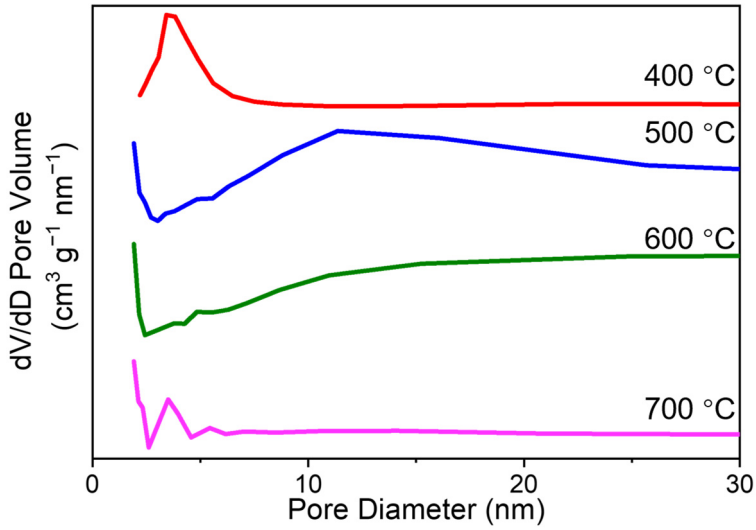


**Supplementary Figure 7 Pore diameter distributions of CoMn-MOCs samples.** Pore diameter distributions of CoMn-MOCs samples obtained at various pretreatment temperatures.

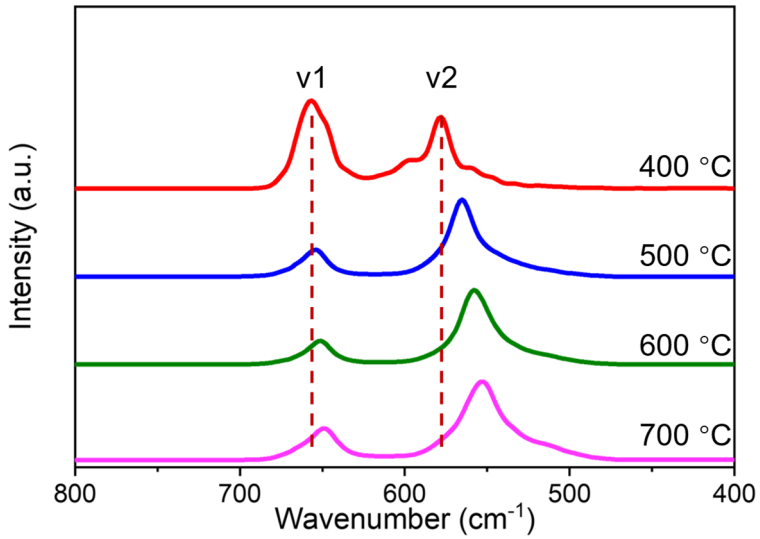


**Supplementary Figure 8 Structure characterizations of CoMn-MOCs samples.** Infrared spectra of CoMn-MOCs samples obtained at various pretreatment temperatures.

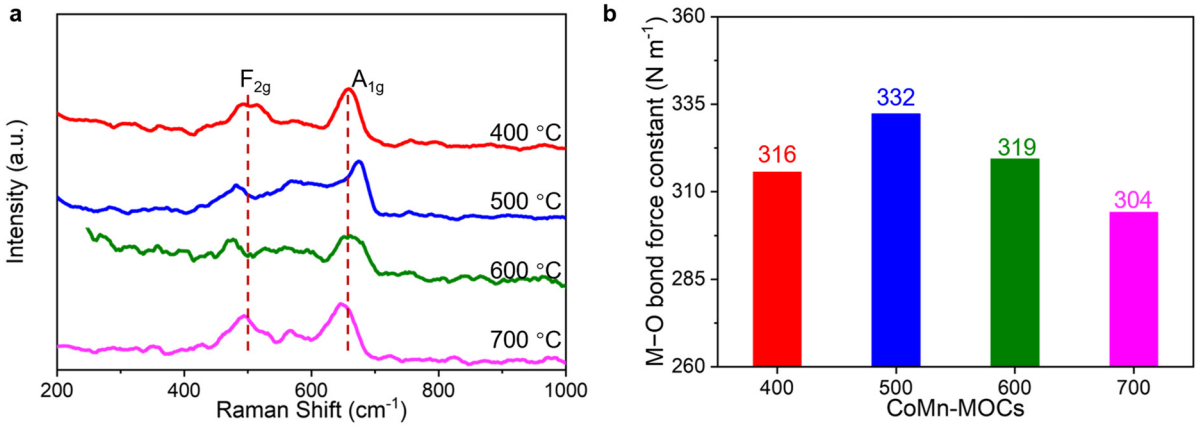


137

138 **Supplementary Figure 9 Raman characterizations of CoMn-MOCs samples. a** Raman

139 spectra of CoMn-MOCs samples, and **b** the calculated M−O bond force constant based on

140 Hooke's law[8].

141

142

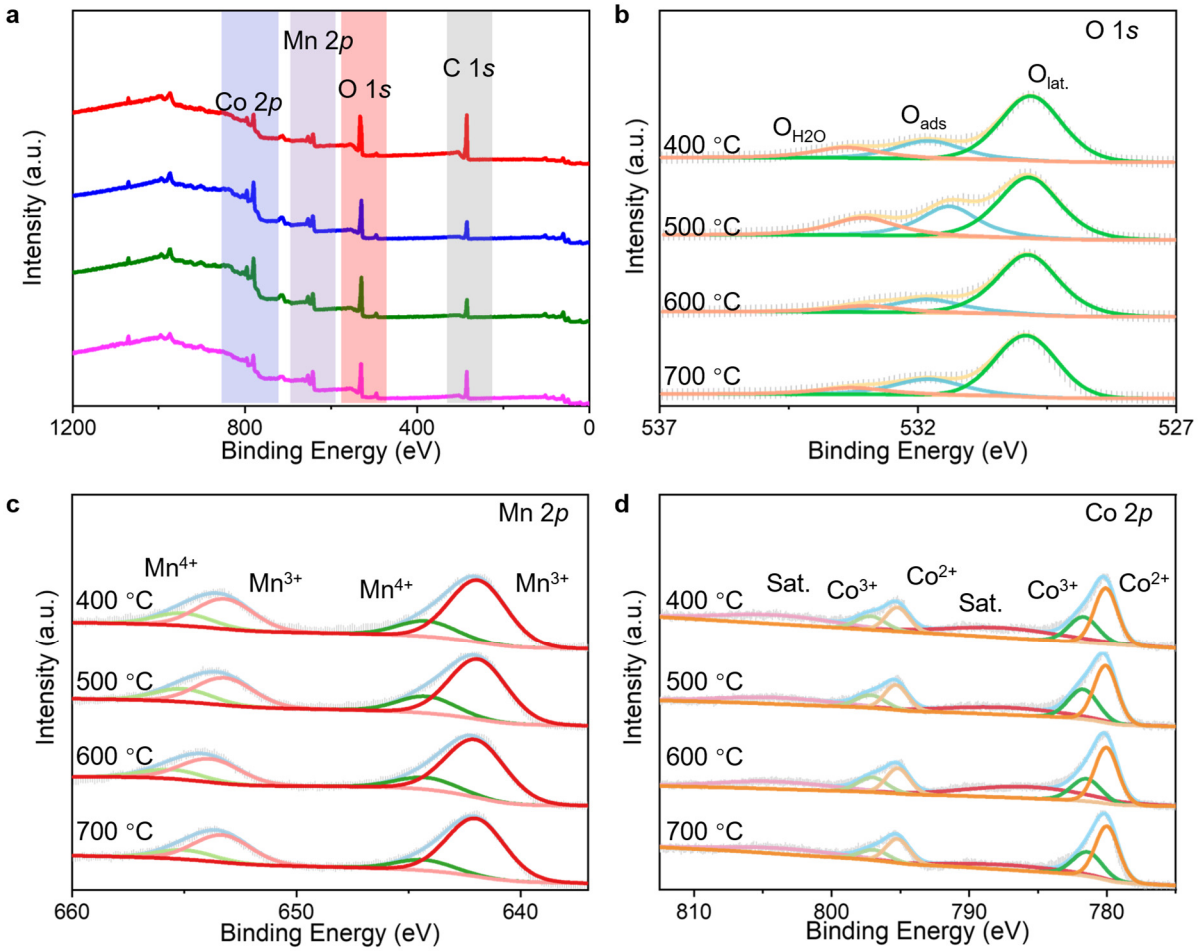


**Supplementary Figure 10 Electronic structure characterizations of CoMn-MOCs samples.** XPS spectra of **a** wide, **b** O 1*s*, **c** Mn 2*p* and **d** Co 2*p* for CoMn-MOCs samples obtained at various pretreatment temperatures.

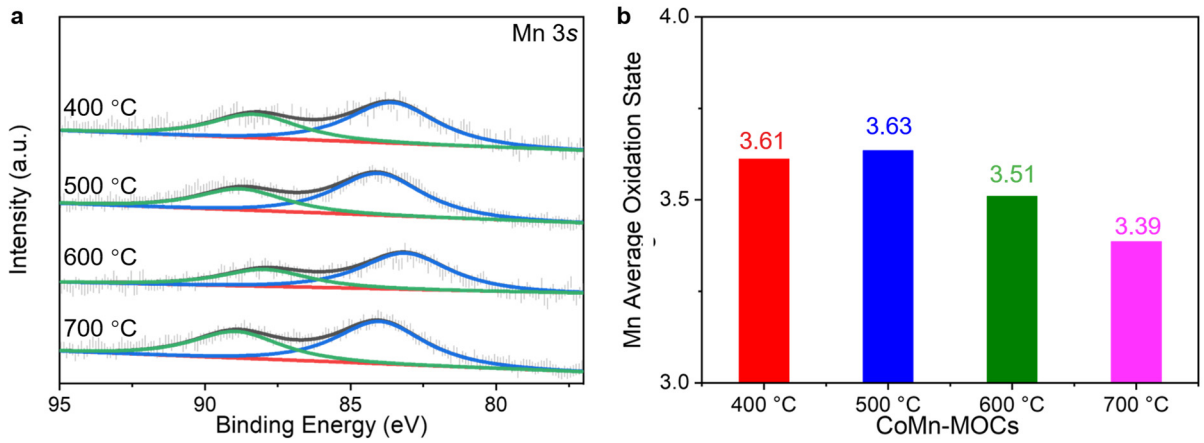


**Supplementary Figure 11 Mean valance of manganese in CoMn-MOCs samples. a** XPS spectra of Mn 3*s* and **b** Mn average oxidation state in CoMn-MOCs samples. The Mn average oxidation state (AOS) is determined through the exchange splitting of Mn 3*s* spectra ($\Delta E_{3s}$) according to the linear equation: AOS = 8.956 − 1.13 $(\Delta E_{3s})$[9].

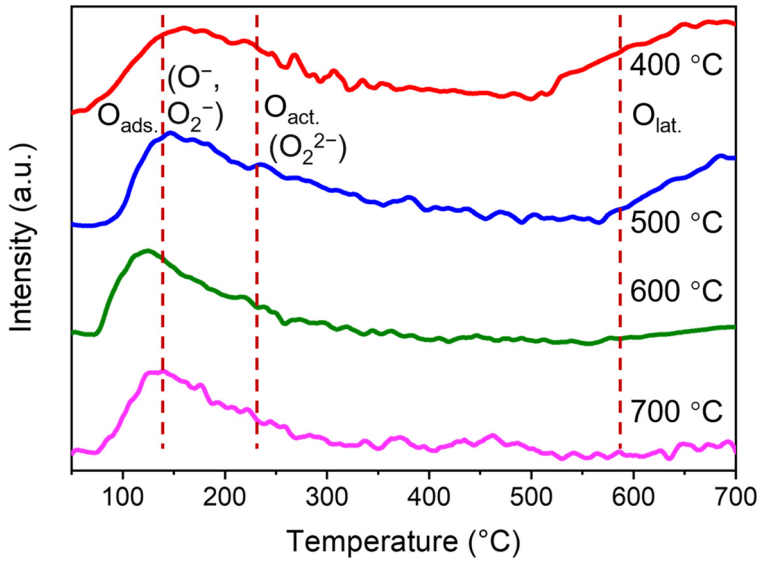


**Supplementary Figure 12 Molecular oxygen activation characterization over CoMn-MOCs samples.** $O_2$-TPD profiles of CoMn-MOCs samples obtained at various pretreatment temperatures.

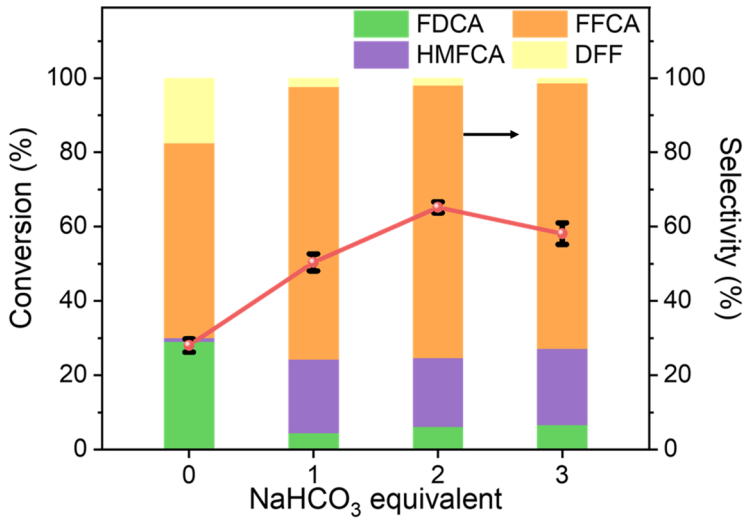


**Supplementary Figure 13 Screening of $NaHCO_3$ equivalent for the catalytic reaction.** Correlation between catalytic performance of CoMn-MOCs-500 and reaction conditions: HMF conversion and product selectivity (HMFCA, DFF, FFCA and FDCA) as function of $NaHCO_3$ equivalent.

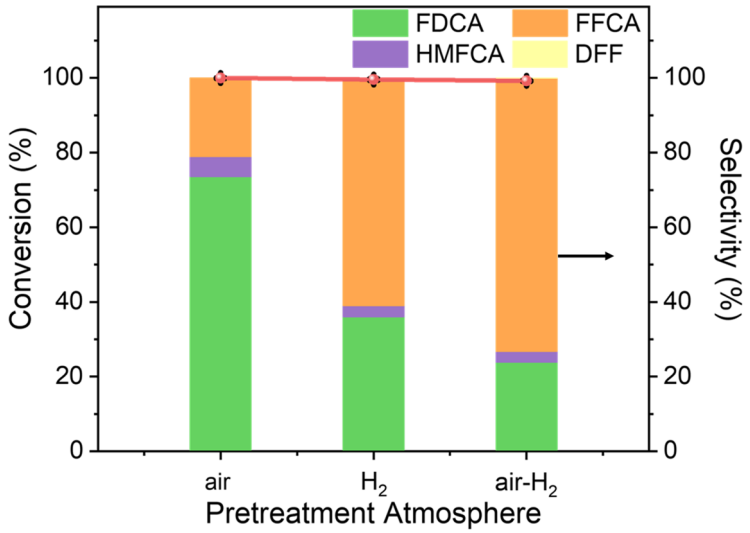


**Supplementary Figure 14 Screening of pretreatment atmosphere for CoMn-MOCs-500.** Correlation between catalytic performance of CoMn-MOCs-500 and reaction conditions: HMF conversion and product selectivity (HMFCA, DFF, FFCA and FDCA) as function of pretreatment atmosphere.

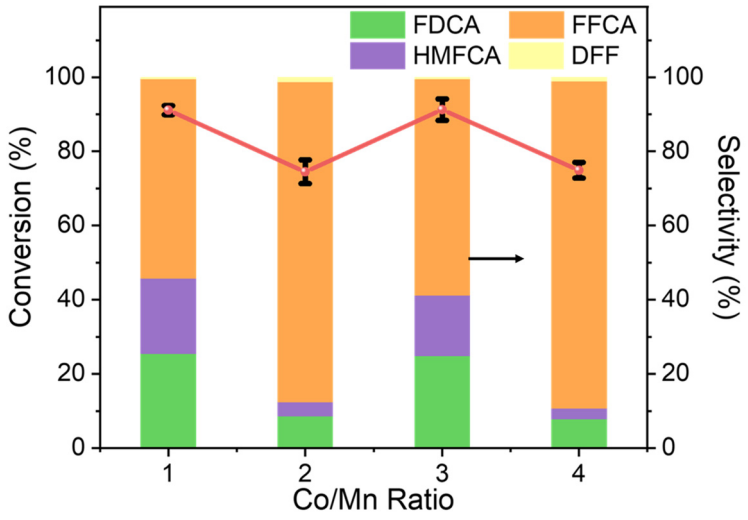


**Supplementary Figure 15 Screening of Co/Mn ratio of CoMn-MOCs-500.** Correlation between catalytic performance of CoMn-MOCs-500 and Co/Mn ratio: HMF conversion and product selectivity (HMFCA, DFF, FFCA and FDCA) as function of Co/Mn ratio.

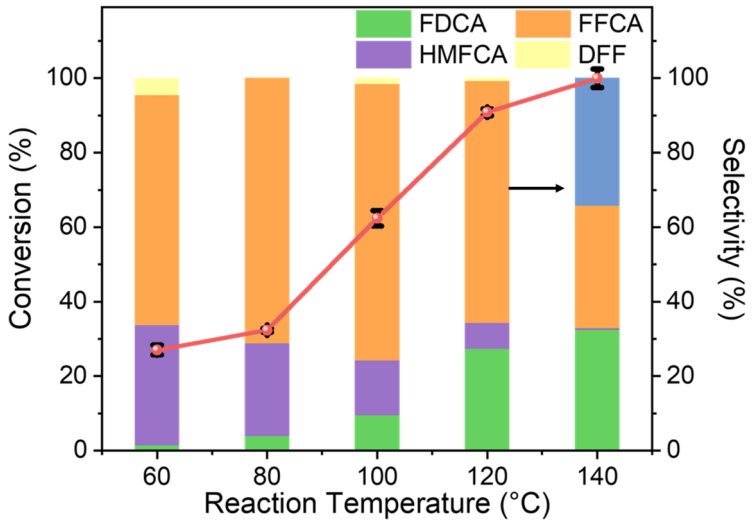


**Supplementary Figure 16 Screening of reaction temperature for the catalytic reaction.** Correlation between catalytic performance of CoMn-MOCs-500 and reaction conditions: HMF conversion and products selectivity (HMFCA, DFF, FFCA and FDCA) as function of reaction temperature.

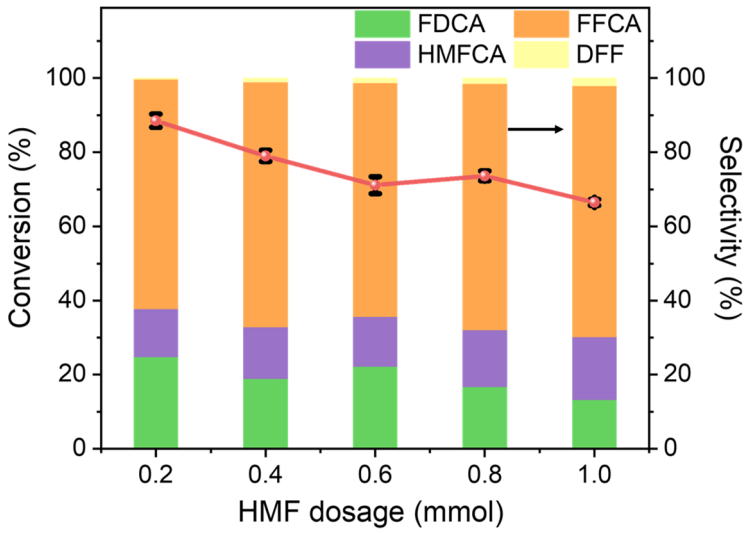


**Supplementary Figure 17 Screening of HMF dosage for the catalytic reaction.** Correlation between catalytic performance of CoMn-MOCs-500 and reaction conditions: HMF conversion and products selectivity (HMFCA, DFF, FFCA and FDCA) as function of HMF dosage.

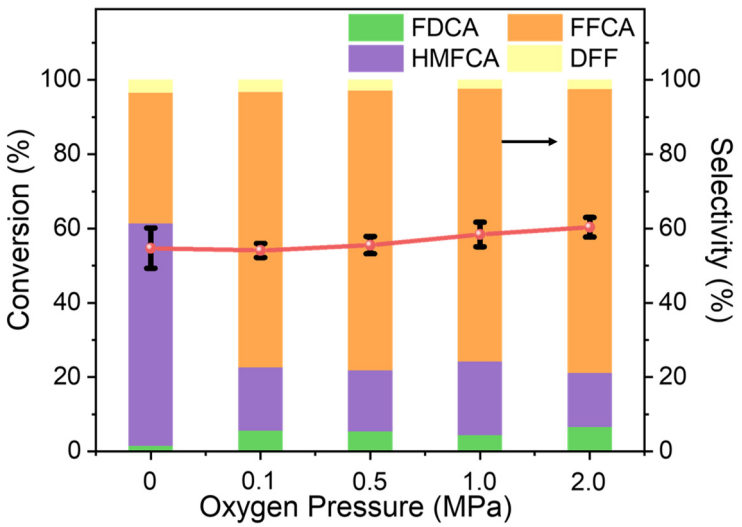


**Supplementary Figure 18 Screening of oxygen pressure for the catalytic reaction.** Correlation between catalytic performance of CoMn-MOCs-500 and reaction conditions: HMF conversion and products selectivity (HMFCA, DFF, FFCA and FDCA) as function of oxygen pressure.

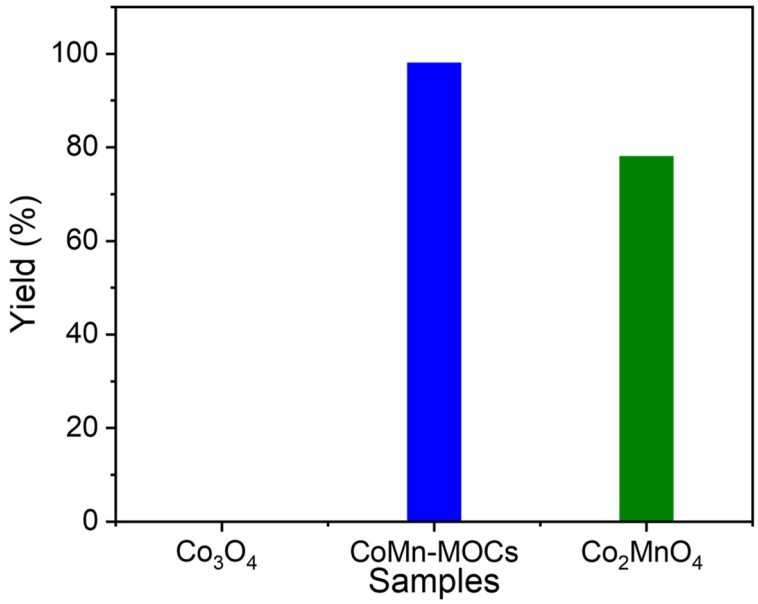


202

203 **Supplementary Figure 19 Catalytic performance of $Co_3O_4$, CoMn-MOCs-500 and**

204 **$Co_2MnO_4$ samples.** FDCA yield over $Co_3O_4$, CoMn-MOCs-500 and $Co_2MnO_4$.

205

206

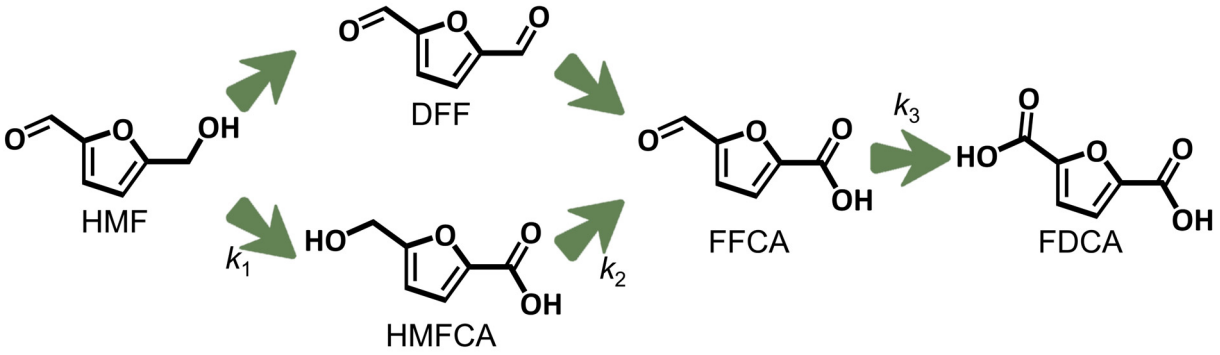


**Supplementary Figure 20 Reaction pathways for the oxidation of HMF to FDCA.** Reaction route with intermediates for the oxidation of HMF to FDCA.

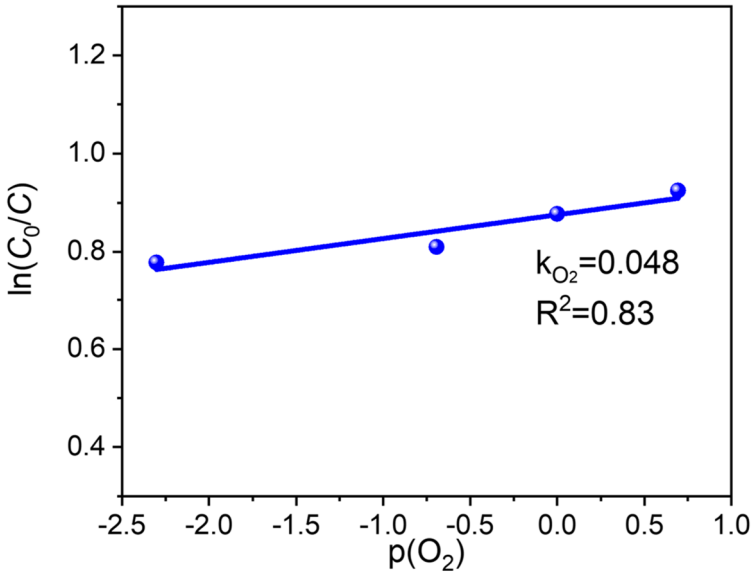


212

213 **Supplementary Figure 21 Tests for internal transport limitations.** Dependence of ln$C/C_0$ of

214 HMF on oxygen pressure (MPa) over CoMn-MOCs-500 catalyst.

215

216

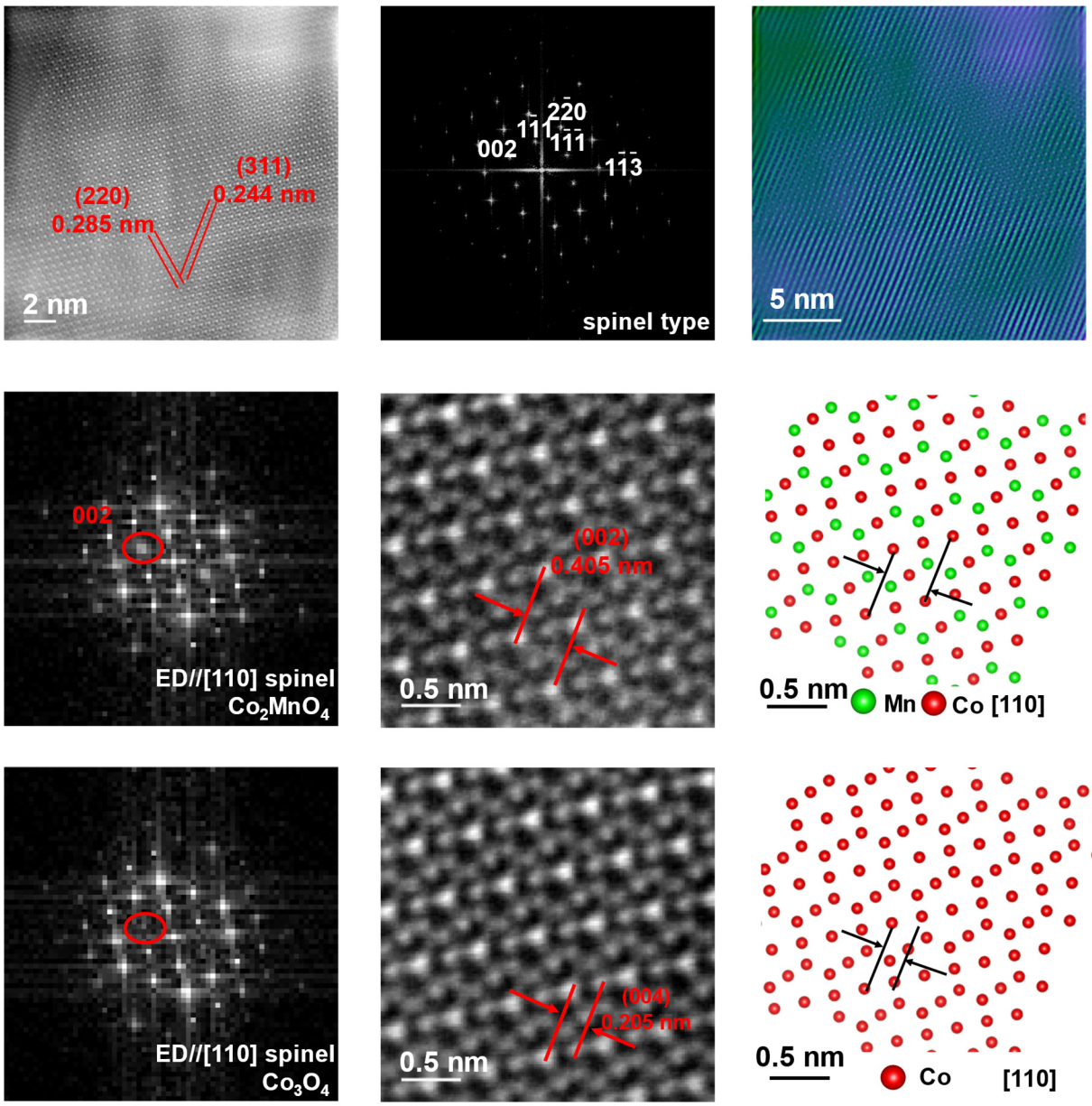


**Supplementary Figure 22 STEM characterizations on CoMn-MOCs-500 sample.** HAADF-STEM images of CoMn-MOCs-500 viewed down the [110] zone axis with the fast Fourier transform images.

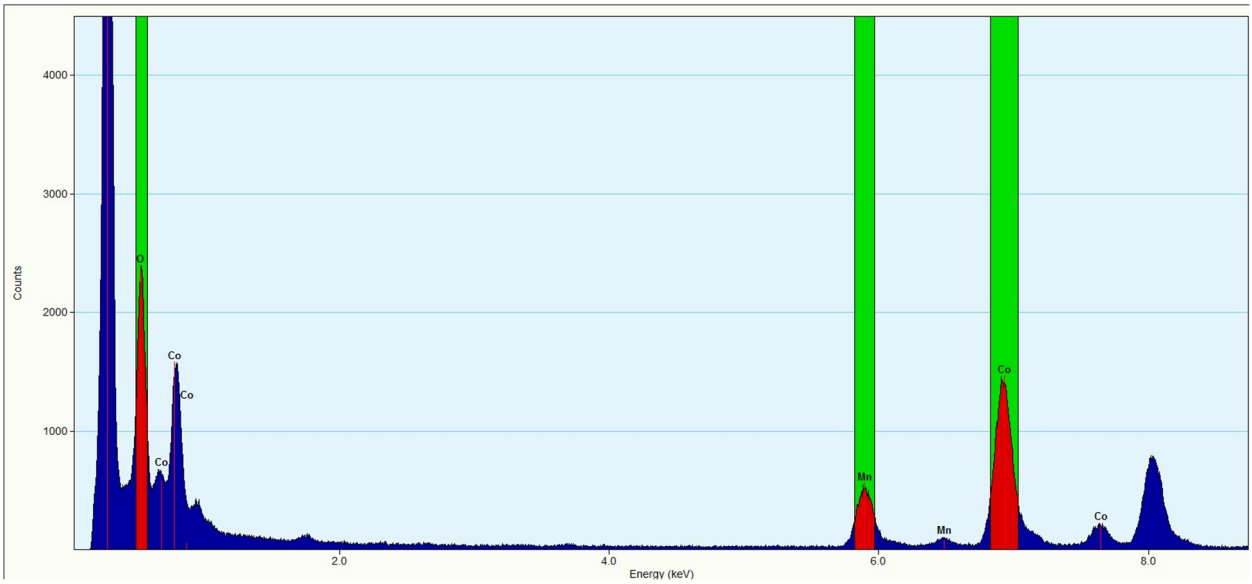


**Supplementary Figure 23 Element distribution of CoMn-MOCs-500.** EDX analysis of CoMn-MOCs-500 sample.

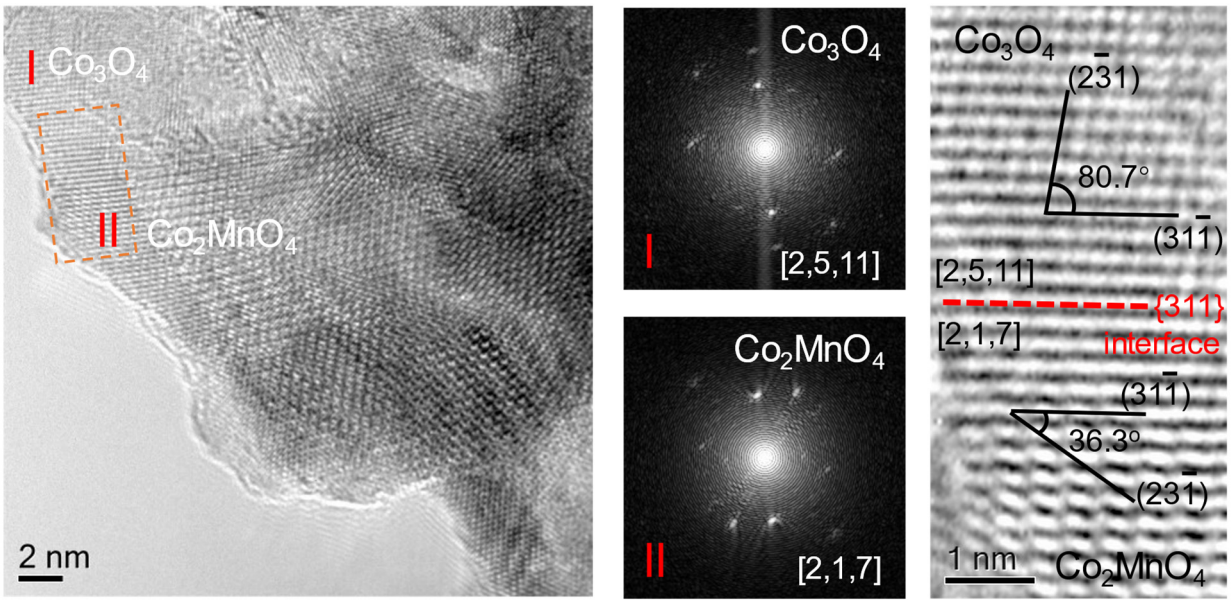


**Supplementary Figure 24 Representative HR-TEM image of CoMn-MOCs-500.** Enlarged HR-TEM images of CoMn-MOCs-500 at the interface between $Co_3O_4$ and $Co_2MnO_4$, along with fast Fourier transform (FFT) patterns.

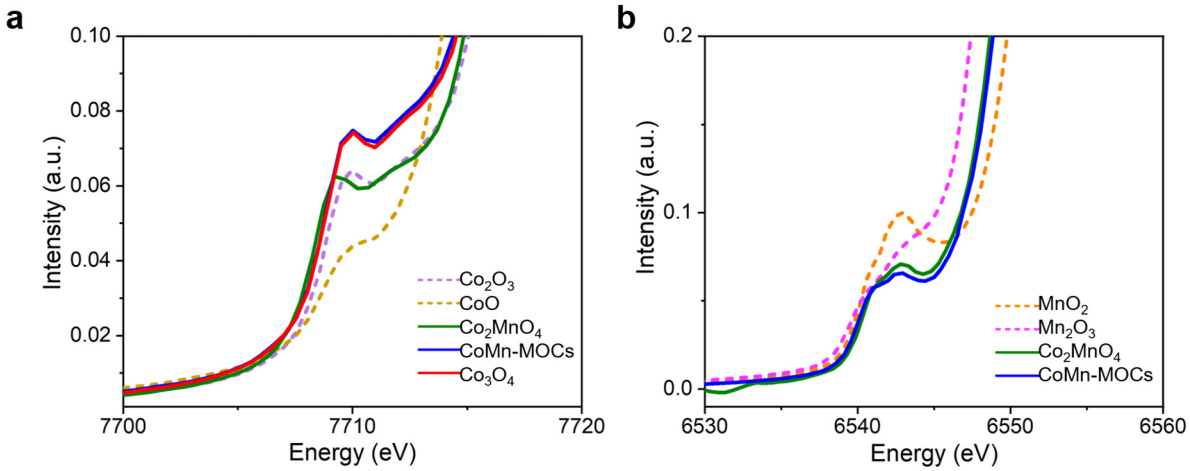


**Supplementary Figure 25 XANES spectra.** Pre-edge of XANES spectra at the **a** Co K-edge of Co-based samples, **b** Mn K-edge of Mn-based samples[10].

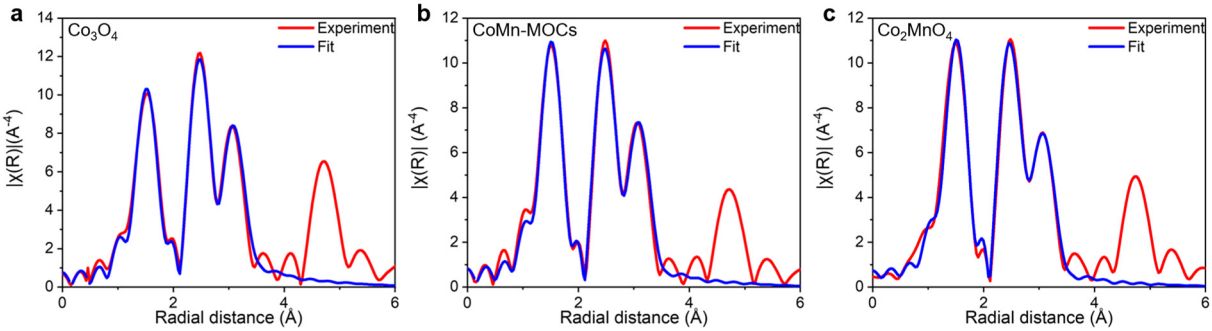


**Supplementary Figure 26 EXAFS spectra Co K-edge.** Fourier-transform EXAFS spectra and fitting at Co K-edge for **a** $Co_3O_4$, **b** CoMn-MOCs-500, and **c** $Co_2MnO_4$.

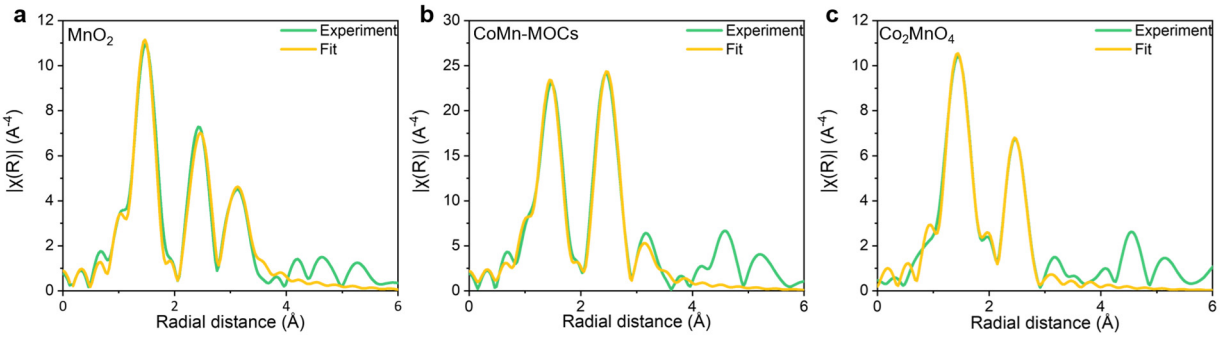


**Supplementary Figure 27 EXAFS spectra of Mn K-edge.** Fourier-transform EXAFS spectra and fitting at Mn K-edge for **a** $MnO_2$, **b** CoMn-MOCs-500, and **c** $Co_2MnO_4$.

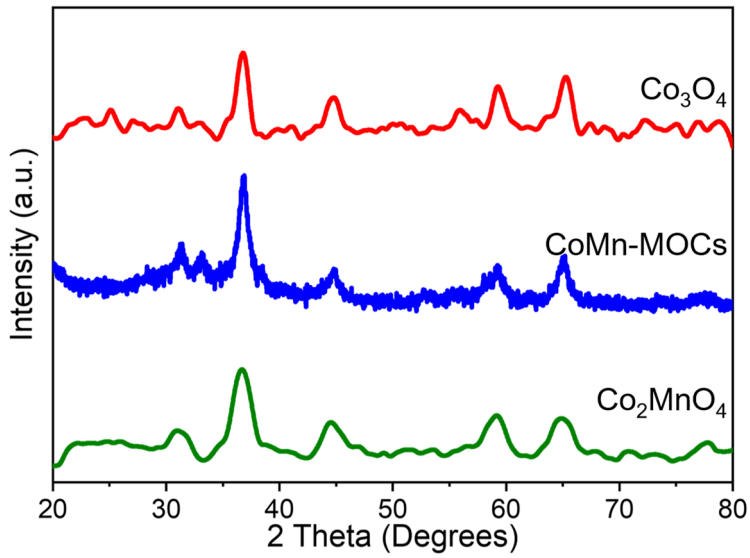


**Supplementary Figure 28 Structure characterizations.** XRD patterns of $Co_3O_4$, CoMn-MOCs-500 and $Co_2MnO_4$ samples.

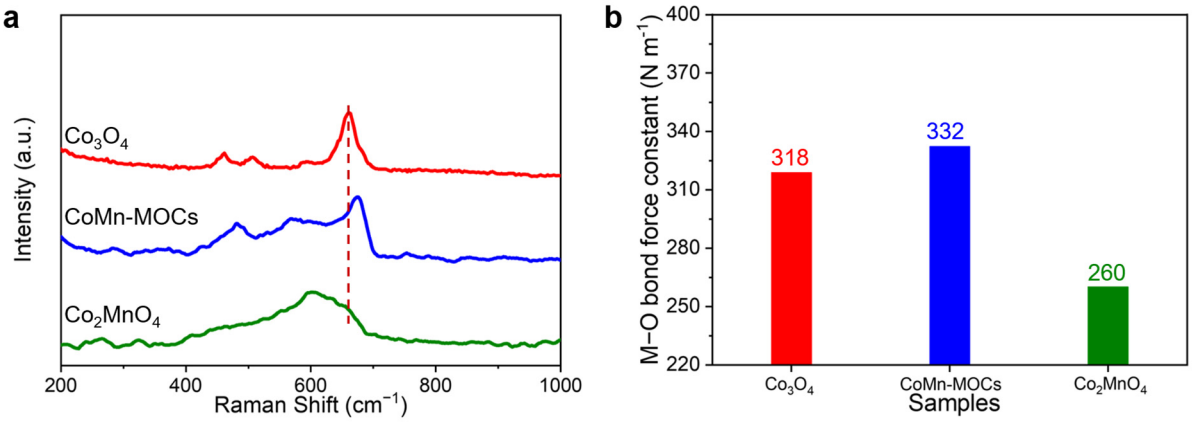


**Supplementary Figure 29 Raman characterizations.** **a** Raman spectra of $Co_3O_4$, CoMn-MOCs-500 and $Co_2MnO_4$, and **b** the calculated M−O bond force constant based on Hooke's law.

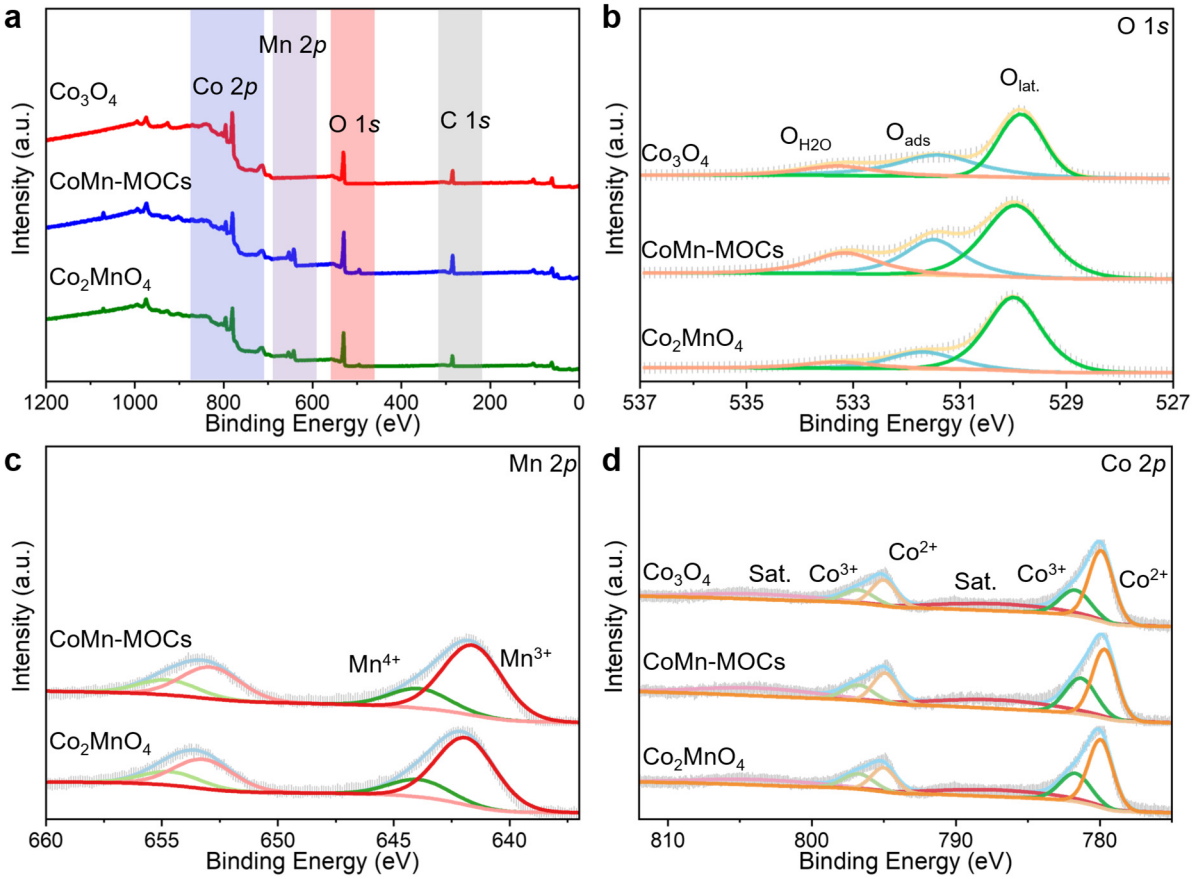


**Supplementary Figure 30 Electronic structure characterizations.** XPS spectra of **a** wide, **b** O 1*s*, **c** Mn 2*p* and **d** Co 2*p* for $Co_3O_4$, CoMn-MOCs-500 and $Co_2MnO_4$, respectively.

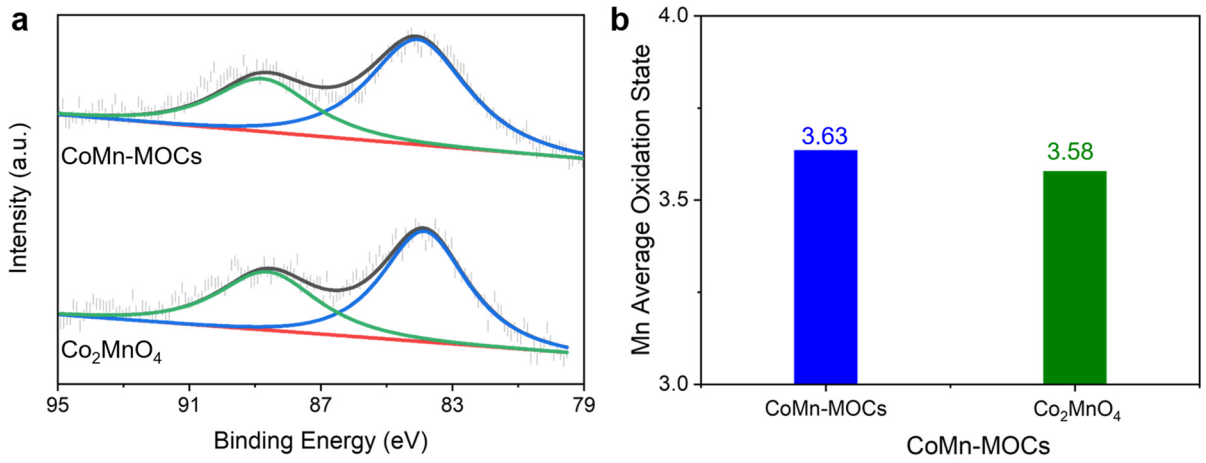


**Supplementary Figure 31 Mean valance of manganese in CoMn-MOCs-500 and $Co_2MnO_4$.** **a** XPS spectra of Mn 3*s* and **b** Mn average oxidation state in CoMn-MOCs-500 and $Co_2MnO_4$. The Mn average oxidation state (AOS) is determined through the exchange splitting of Mn 3*s* spectra ($\Delta E_{3s}$) according to the linear equation: AOS = 8.956 − 1.13 ($\Delta E_{3s}$).

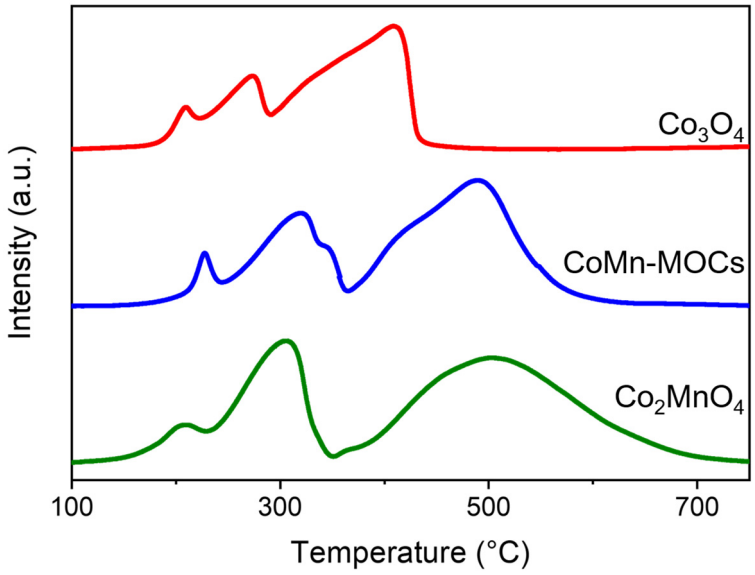


**Supplementary Figure 32 Surface reducibility tests of $Co_3O_4$, CoMn-MOCs-500 and $Co_2MnO_4$.** $H_2$-TPR profiles of $Co_3O_4$, CoMn-MOCs-500 and $Co_2MnO_4$, respectively.

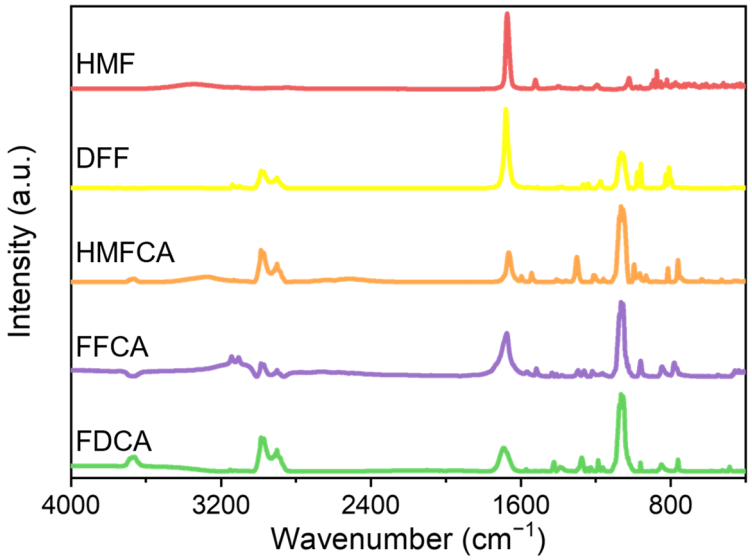


277

278 **Supplementary Figure 33 Infrared spectra of reactants and oxidation products.** FT-IR

279 spectra of HMF, DFF, HMFCA, FFCA and FDCA, respectively[11].

280

281

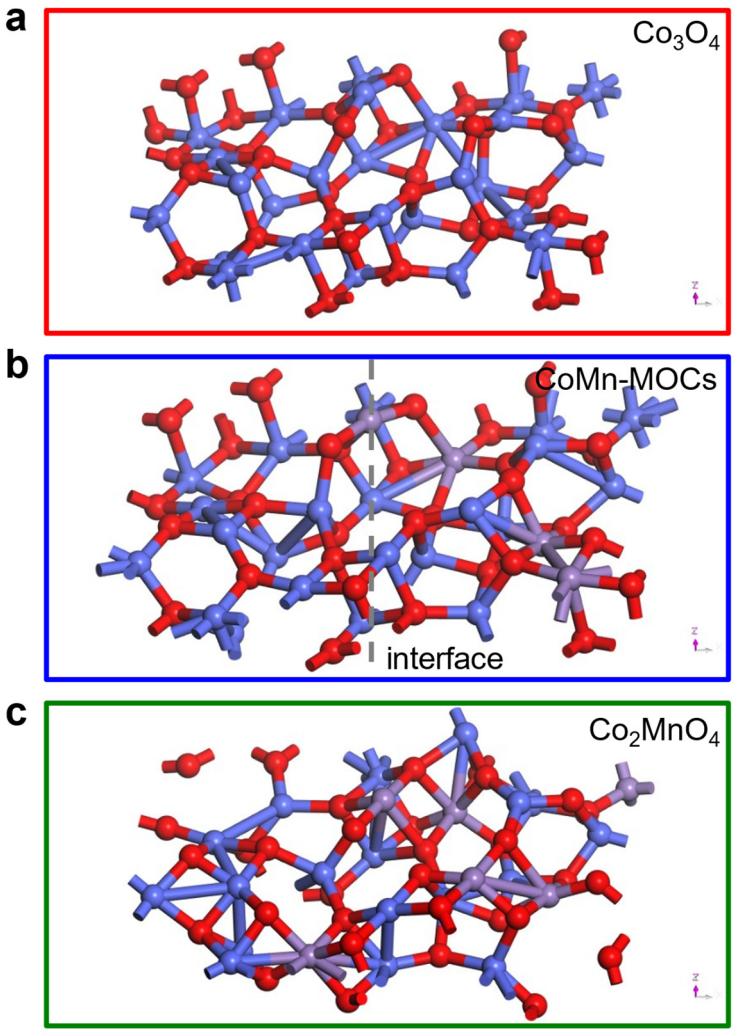


**Supplementary Figure 34 Structure models.** Structure models of **a** $Co_3O_4$(311), **b** CoMn-MOCs(311) and **c** $Co_2MnO_4$(311) surface.

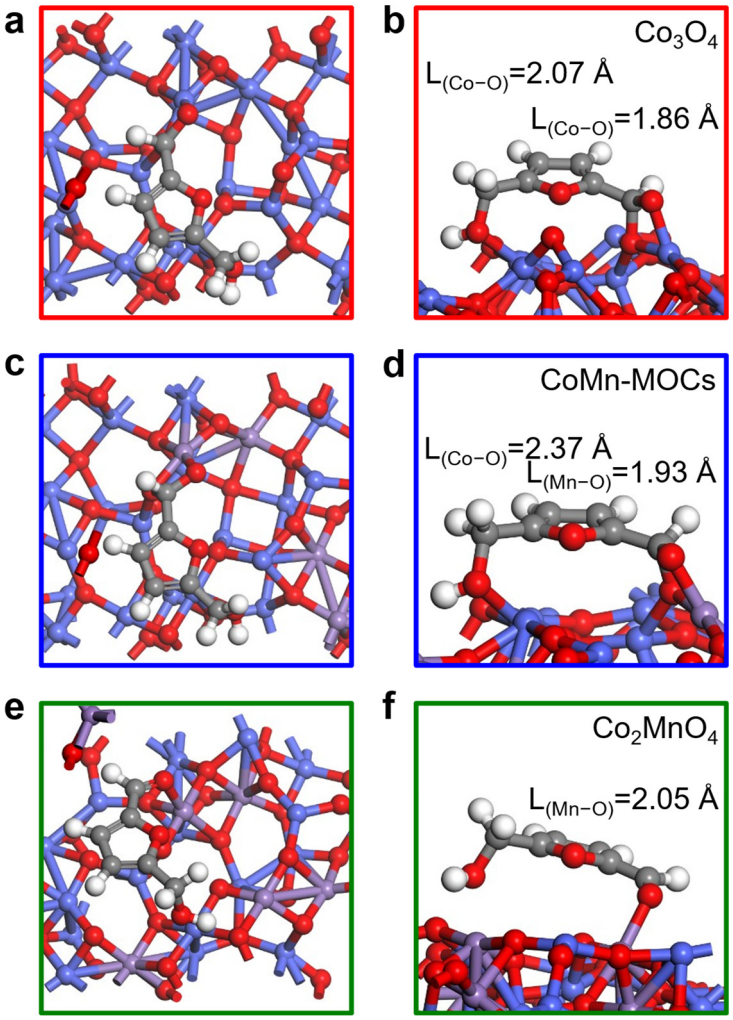


**Supplementary Figure 35 Adsorption configurations of HMF.** Optimized adsorption configurations of HMF with calculated M−O (oxygen from carbon-oxygen bond) bond length on **a, b** $Co_3O_4$(311), **c, d** CoMn-MOCs(311), **e, f** $Co_2MnO_4$(311) surface.

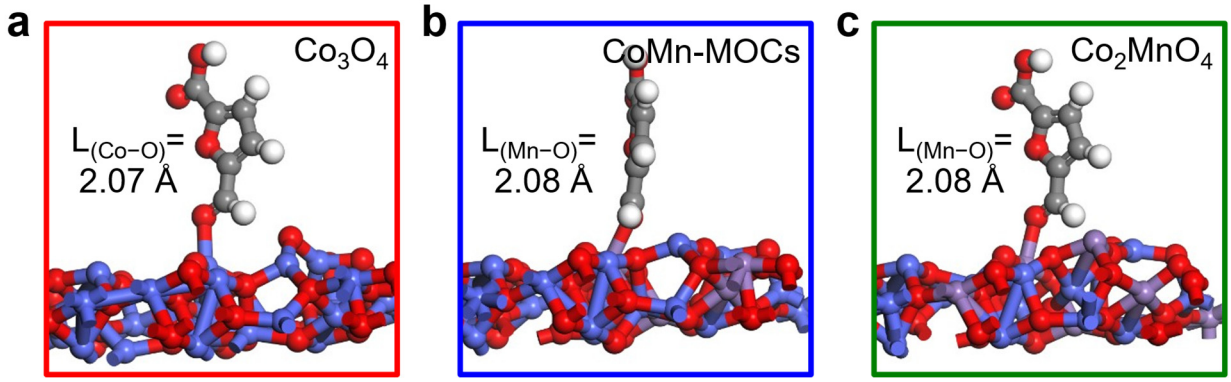


**Supplementary Figure 36 Adsorption configurations of FFCA.** Optimized adsorption configurations of FFCA with calculated M−O (oxygen from C=O bond) bond length on **a** $Co_3O_4$(311), **b** CoMn-MOCs(311), **c** $Co_2MnO_4$(311) surface.

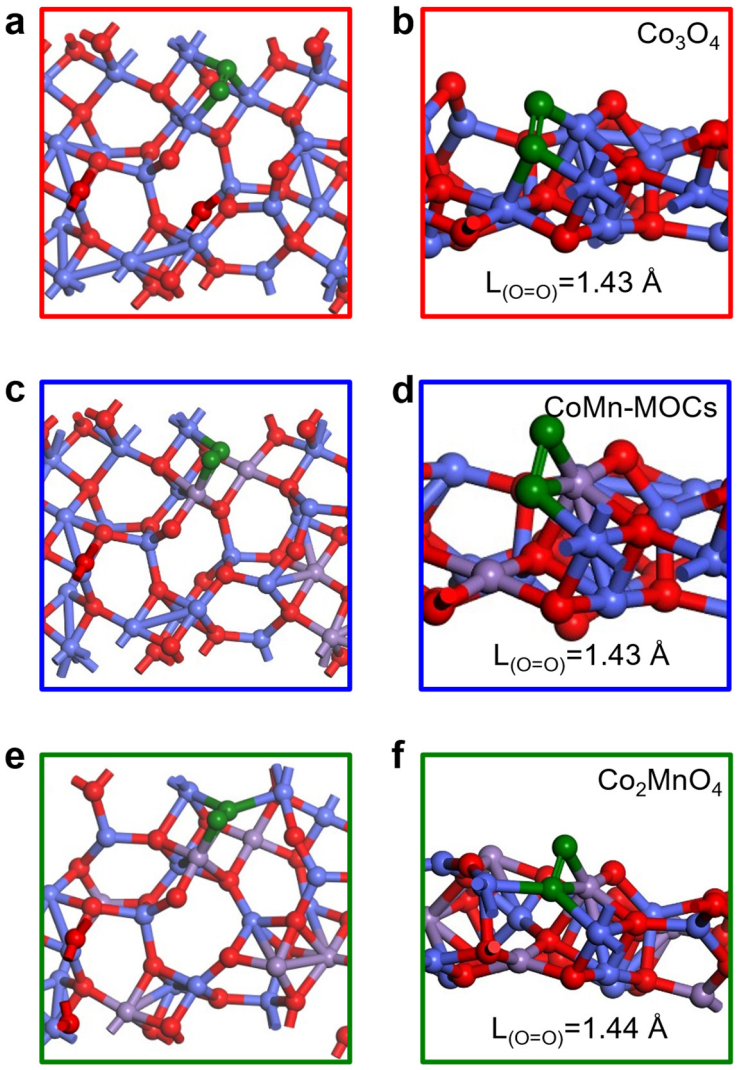


**Supplementary Figure 37 Adsorption configurations of oxygen at oxygen vacancy.** Optimized adsorption configurations of oxygen at oxygen vacancy with calculated O=O bond length on **a, b** $Co_3O_4$(311), **c, d** CoMn-MOCs(311), **e, f** $Co_2MnO_4$(311) surface.

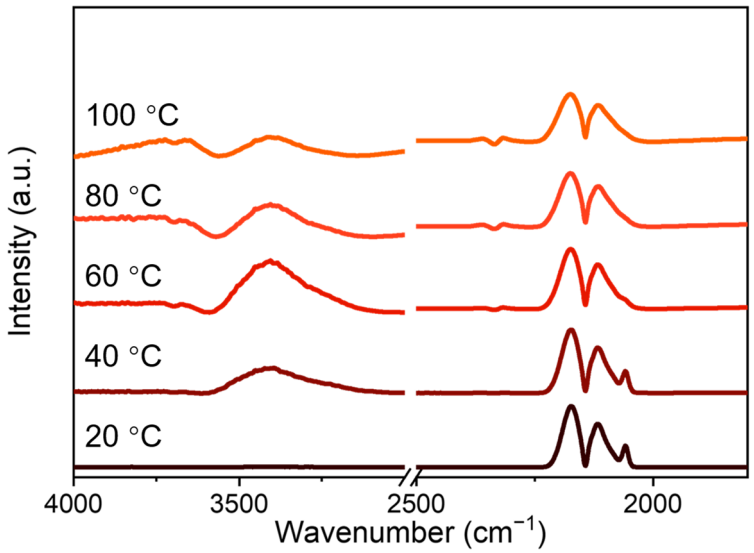


**Supplementary Figure 38 *In situ* investigations on CO adsorption.** FT-IR spectra of CO adsorption on CoMn-MOCs-500 at different temperatures.

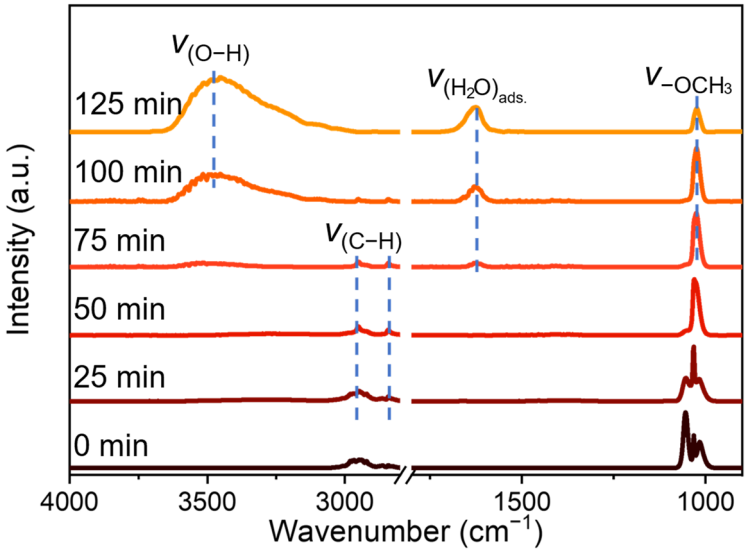


310

311 **Supplementary Figure 39 *In situ* investigations on methanol adsorption.** FT-IR spectra of

312 $CH_3OH$ adsorption on CoMn-MOCs-500.

313

314

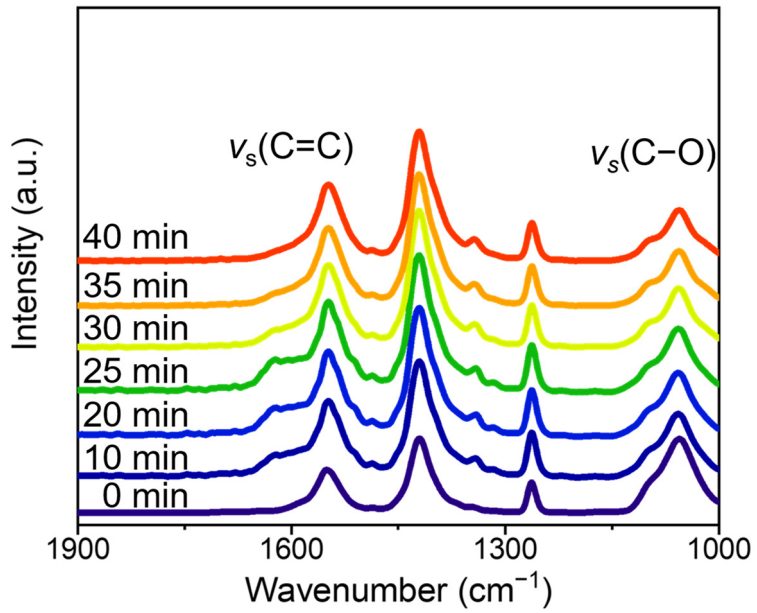


315

316 **Supplementary Figure 40 *In situ* investigations on DFF oxidation.** *In situ* FT-IR spectra of

317 DFF oxidation on CoMn-MOCs-500.

318

319

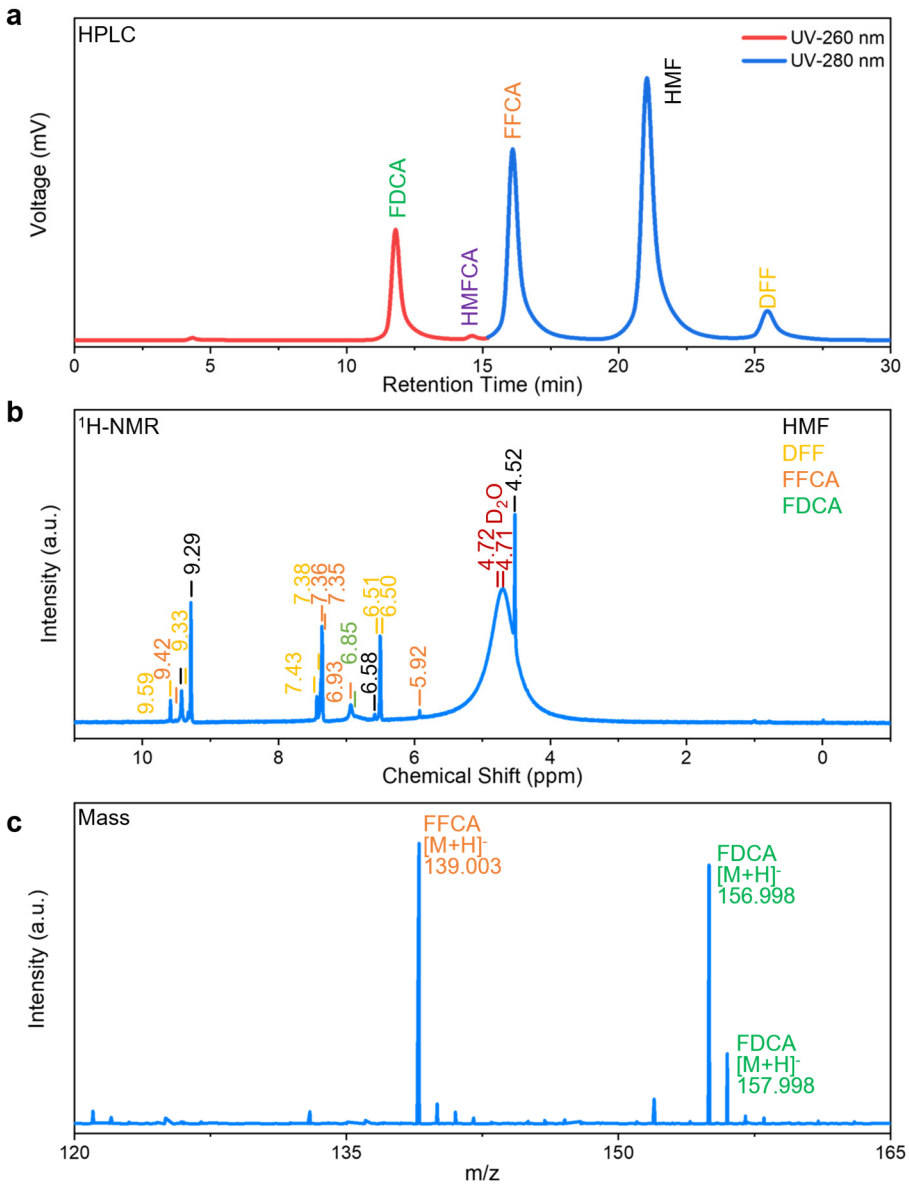


**Supplementary Figure 41 Investigations on reaction paths. a** HPLC data based on UV detector, **b** $^{1}$H-NMR analysis[12], and **c** mass spectra (electronegative ion mode) of deuterium-labeled HMF and its derivatives. Reaction conditions: 0.1 g of CoMn-MOCs-500, 0.20 mmol of HMF, 20 mL of $D_2O$, 120 °C, 0.1 MPa $O_2$, base free, 12 h.

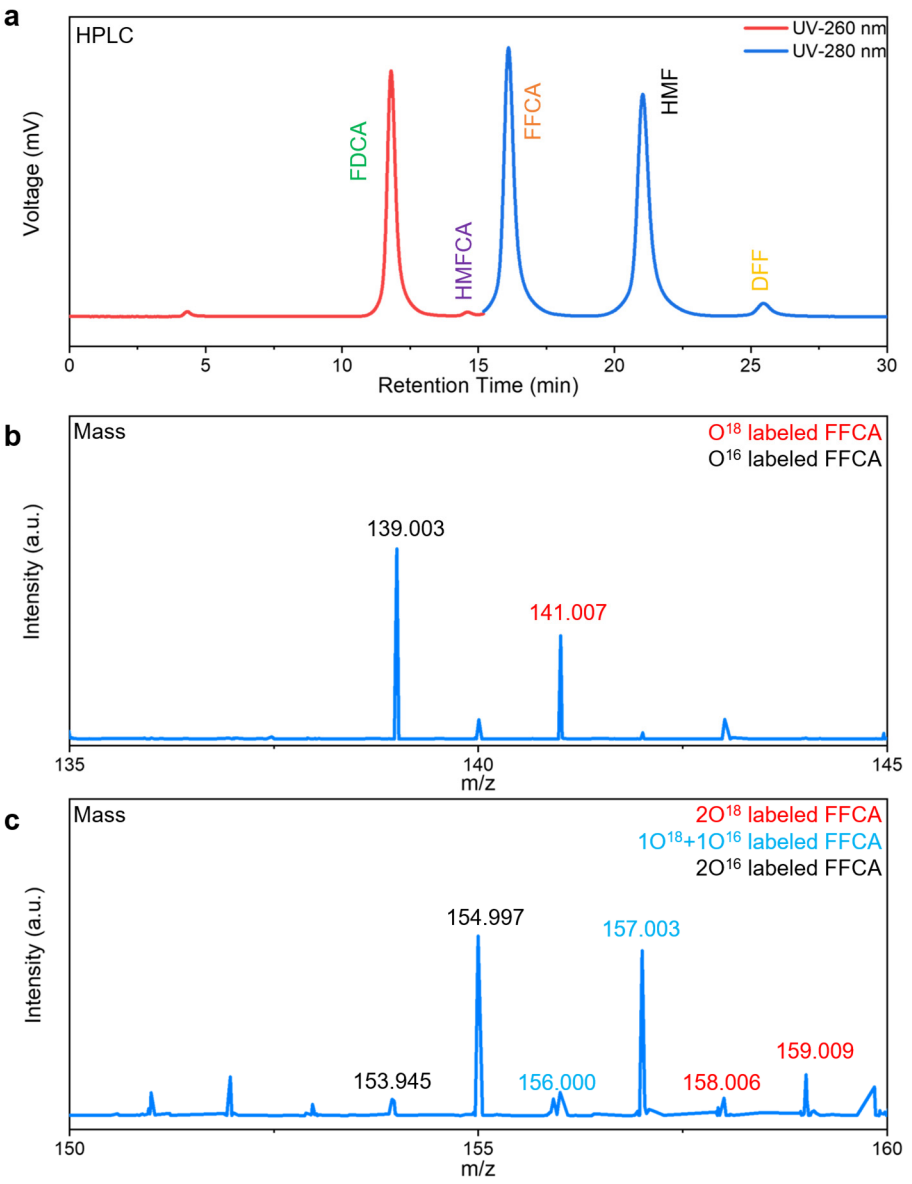


**Supplementary Figure 42 Investigations on the source of oxygen. a** HPLC data based on UV detector, and mass spectra (electronegative ion mode) of $^{18}O$-labeled **b** FFCA and **c** FDCA. Reaction conditions: 0.1 g of CoMn-MOCs-500, 0.20 mmol of HMF, $H_2O$ (5 mL) + $H_2O^{18}$ (1 mL), 120 °C, 0.1 MPa $O_2$, base free, 12 h.

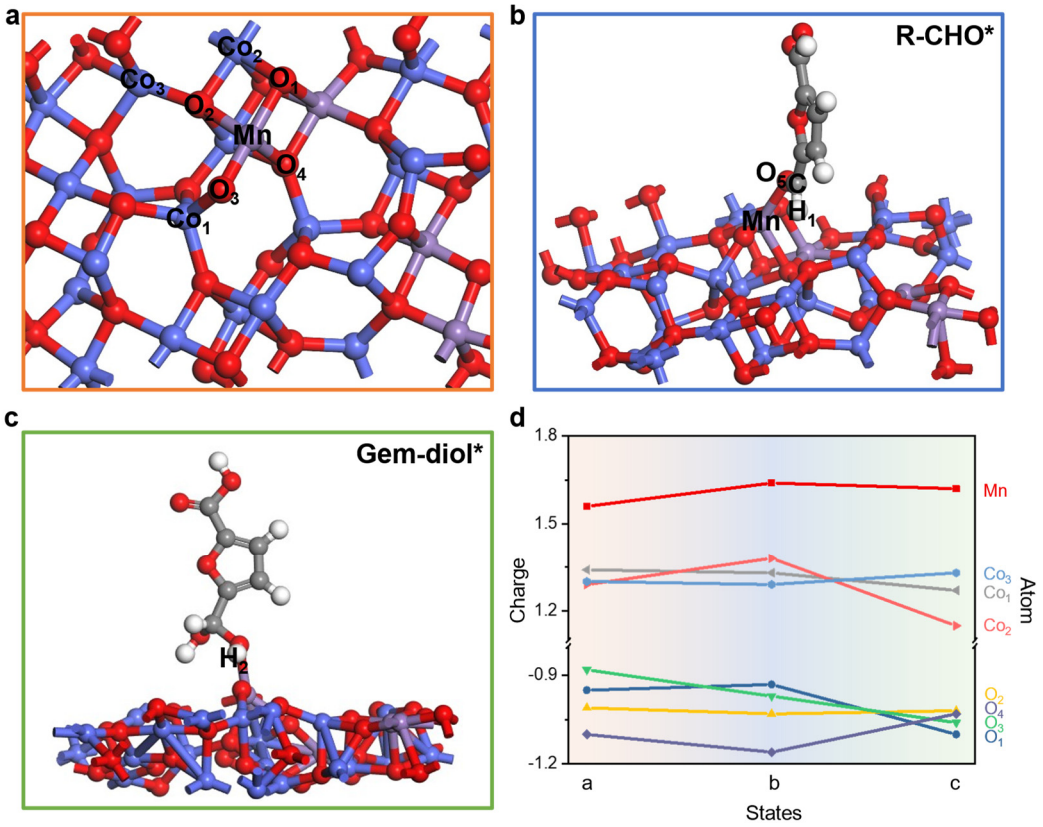


334

335 **Supplementary Figure 43 Studies on electronic structure.** Bader charge analysis of **a**
336 CoMn-MOCs-500, **b** CoMn-MOCs-500 with adsorbed FFCA and **c** CoMn-MOCs-500 with
337 adsorbed gem-diol. **d** Plots for Bader charge of Co, Mn, O *vs* different catalytic states from **a**, **b**,
338 **c**.

339

340

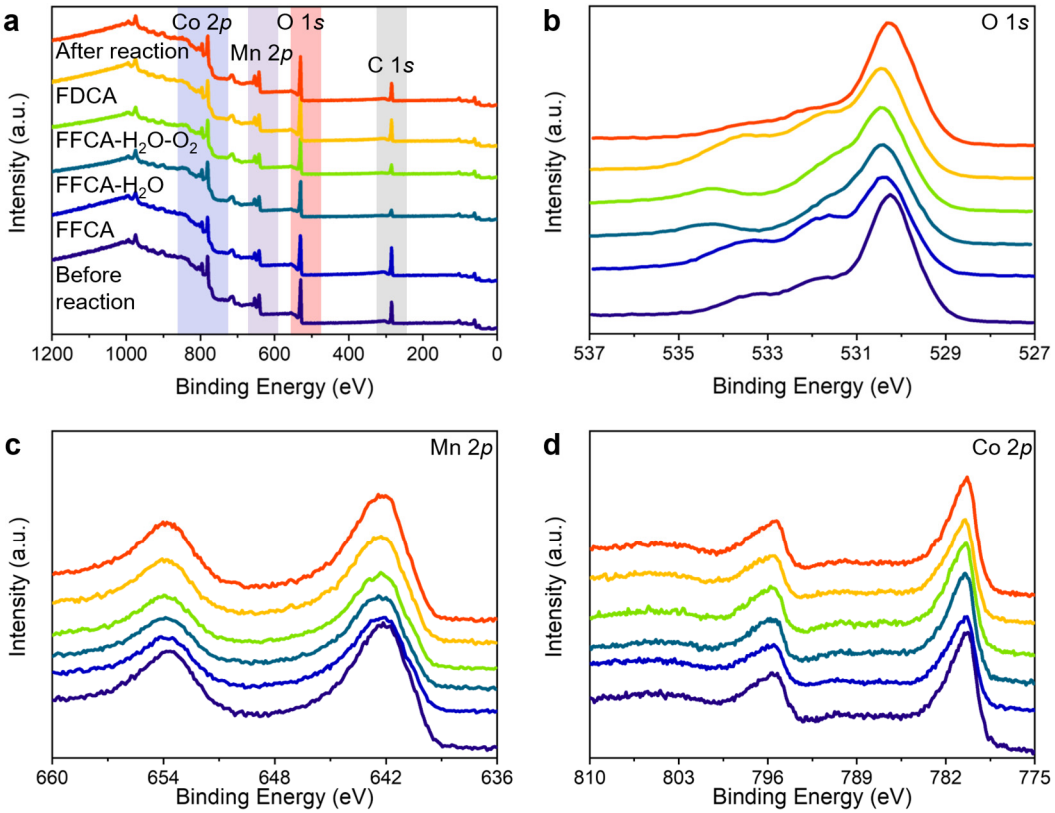


341

342 **Supplementary Figure 44 Electronic structure characterizations on the oxidation process of**
343 **FFCA over CoMn-MOCs-500.** *Quasi in situ* XPS spectra of **a** wide, **b** O 1*s*, **c** Mn 2*p* and **d** Co
344 2*p*.

345

346

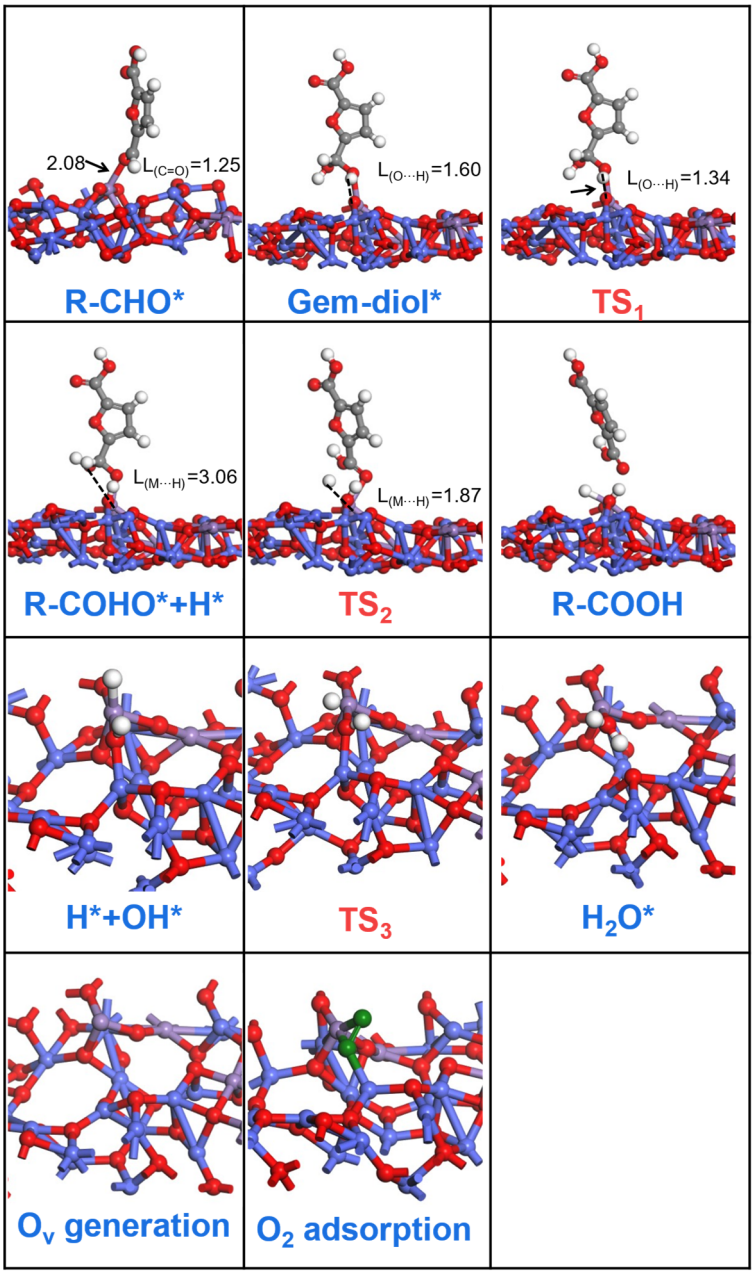


**Supplementary Figure 45 Studies on FFCA oxidation on the surface of CoMn-MOCs.** Geometric configurations for the elementary reaction steps of FFCA oxidation to FDCA on CoMn-MOCs, along with the transition state (TS), intermediate and final state (FS). '*' represents the adsorption state of the adsorbate.

# Supplementary Tables

**Supplementary Table 1 Physicochemical parameters of CoMn-MOCs samples**

| Sample | Specific surface area ($m^2\ g^{-1}$)[a] | Pore volume ($cm^3\ g^{-1}$)[a] | Pore size (nm)[a] |
|---|---|---|---|
| CoMn-MOCs-400 | 91.1 | 0.03 | 10.4 |
| CoMn-MOCs-500 | 53.5 | 2.33 | 20.7 |
| CoMn-MOCs-600 | 34.6 | 1.95 | 30.0 |
| CoMn-MOCs-700 | 15.6 | 2.12 | 15.0 |

[a] Specific surface area, pore volume and pore size were determined by BET.

**Supplementary Table 2 FT-IR/Raman characterizations on M−O bond**

| Sample | Intensity ratio of v1:v2 stretching mode | Raman shift of $A_{1g}$ ($cm^{-1}$) | M−O bond Force constant[a] |
|---|---|---|---|
| CoMn-MOCs-400 | 0.54 : 0.46 | 658 | 316 |
| CoMn-MOCs-500 | 0.27 : 0.73 | 675 | 332 |
| CoMn-MOCs-600 | 0.26 : 0.74 | 662 | 319 |
| CoMn-MOCs-700 | 0.30 : 0.70 | 646 | 304 |

[a] Intensity ratio of ν1:ν2 stretching mode was calculated from the vibration frequency of the characteristic bands in FT-IR spectra[13].

[b] M−O bond force constant was calculated by Hooke's law: $\omega = \frac{1}{2\pi c}\sqrt{\frac{k}{\mu}}$.

**Supplementary Table 3 Quantitative results of $H_2$-TPR**

| Sample | $H_2$ consumption (mmol $g^{-1}$)[a] | | | Total $H_2$ consumption (mmol $g^{-1}$) | Theoretical $H_2$ consumption (mmol $g^{-1}$) |
|---|---|---|---|---|---|
| | < 280 °C | 300−400 °C | > 500 °C | | |
| CoMn-MOCs-400 | 1.7 | 8.7 | 7.0 | 17.3 | 31.6 |
| CoMn-MOCs-500 | 2.0 | 8.3 | 13.2 | 23.5 | 32.0 |
| CoMn-MOCs-600 | 1.5 | 7.6 | 12.0 | 21.2 | 31.7 |
| CoMn-MOCs-700 | 1.3 | 6.1 | 12.0 | 19.4 | 31.7 |

[a] $H_2$ consumption was quantified by using $Ag_2O$ as a calibration reference.

**Supplementary Table 4 Comparison of catalytic performance for selective oxidation of HMF over various catalysts**

| Catalyst | Reaction conditions | Con. (%) | FDCA Sel. (%) | Yield (%) | Formation Rate (μmol $g_{metal}^{-1}$ $h^{-1}$)[a] | Ref. |
|---|---|---|---|---|---|---|
| CoMn-MOCs-500 | 120 °C, 0.1 MPa $O_2$, $NaHCO_3$(2 eq) | >99 | 98 | 98 | 488.0 | This work |
| $Mn_3Co_2O_x$–0.3VC | 130 °C, 1.5 MPa air, $NaHCO_3$(2 eq) | 100 | 96 | 96 | / | 14 |
| $CoO_x$-MC | 80 °C, 0.5 MPa air, $NaHCO_3$(3.6 eq) | 98 | 97 | 95 | / | 15 |
| $Mn_2O_3$ | 100 °C, 1.4 MPa $O_2$, $NaHCO_3$(3 eq) | 100 | 99 | 99 | 397.1 | 16 |
| $MnO_2$ | 100 ℃,1 MPa $O_2$, $NaHCO_3$(3 eq) | 100 | 91 | 91 | 240.0 | 17 |
| Co-Mn-0.25 | 120 °C, 2 MPa $O_2$, $NaHCO_3$(2 eq) | 99 | 95 | 94 | / | 18 |
| CuO $MnO_2$ $CeO_2$ | 130 °C, 1 MPa $O_2$, base free | 97 | 69 | 67 | 120.2 | 19 |
| $MnO_2$ | 120 °C,1 MPa $O_2$, $NaHCO_3$(3 eq) | 100 | 95 | 95 | 120.0 | 20 |
| $MnO_x$-$CeO_2$ | 75 °C, 1 MPa $O_2$, $KHCO_3$(4 eq) | 98 | 91 | 89 | / | 21 |
| $Mn_{0.75}Fe_{0.25}$ | 90 °C, 0.8 MPa $O_2$, NaOH (4 eq) | 79 | 9 | 7 | / | 22 |

[a] Formation rate = moles of FDCA product / (moles of active $metal^{-1}$ × $h^{-1}$)

**Supplementary Table 5 Kinetic parameters for HMF oxidation over CoMn-MOCs-500**

| Oxidation reaction | Rate constant ($h^{-1}$)[a] | Rate constant ($h^{-1}$)[b] |
|---|---|---|
| $k_1$ (HMF → HMFCA) | 0.90 | 0.92 |
| $k_2$ (HMFCA → FFCA) | 9.36 | / |
| $k_3$ (FFCA → FDCA) | 0.68 | 0.17 |

[a] Based on the time curve for the oxidation reaction of HMF.

[b] Based on the oxidation reaction of different substrates.

**Supplementary Table 6 Curve-fitting results of Co K-edge EXAFS spectra**

| Sample | Shell | *R* (Å)[a] | *C.N.*[b] | $\sigma^2$ ($10^{-3}$Å$^2$)[c] | $\Delta E_0$ (eV)[d] | *R* factor (%)[e] |
|---|---|---|---|---|---|---|
| $Co_3O_4$ | Co–O | 1.91(0.01) | 3.7(0.3) | 1.8 | 4.6 | 0.7 |
| | Co–Co | 2.86(0.01) | 4.8(1.0) | 5.4 | | |
| | Co–Co | 3.37(0.01) | 5.3(1.3) | 4.6 | | |
| $Co_2MnO_4$ | Co–O | 1.91(0.01) | 4.7(0.4) | 1.8 | 3.8 | 0.6 |
| | Co–M | 2.86(0.01) | 5.2(1.3) | 5.4 | | |
| | Co–M | 3.38(0.01) | 7.2(2.3) | 5.4 | | |
| CoMn-MOCs | Co–O | 1.92(0.01) | 4.3(0.3) | 2.7 | 4.1 | 0.6 |
| | Co–M | 2.87(0.01) | 5.0(1.1) | 6.5 | | |
| | Co–M | 3.39(0.01) | 6.5(1.8) | 6.8 | | |

[a] Bond distance.
[b] Coordination number.
[c] Debye-Waller factor.
[d] The inner potential correction.
[e] Goodness of fit.

**Supplementary Table 7 Curve-fitting results of Mn K-edge EXAFS spectra**

| Sample | Shell | *R* (Å)[a] | *C.N.*[b] | $\sigma^2$ ($10^{-3}$Å$^2$)[c] | $\Delta E_0$ (eV)[d] | *R* factor (%)[e] |
|---|---|---|---|---|---|---|
| $MnO_2$ | Mn–O | 1.89(0.01) | 4.3(0.3) | 3.1 | 0.9 | 0.9 |
| | Mn–Mn | 2.88(0.01) | 3.5(1.4) | 6.8 | | |
| | Mn–Mn | 3.43(0.01) | 1.5(0.2) | 10.3 | | |
| $Co_2MnO_4$ | Mn–O | 1.88(0.01) | 2.2(0.1) | 2.6 | 0.2 | 0.4 |
| | Mn–M | 2.89(0.01) | 2.9(0.6) | 10.2 | | |
| CoMn-MOCs | Mn–O | 1.90(0.01) | 2.0(0.1) | 5.0 | 0.9 | 0.5 |
| | Mn–M | 2.89(0.01) | 6.6(1.0) | 6.8 | | |

[a] Bond distance.

[b] Coordination number.

[c] Debye-Waller factor.

[d] The inner potential correction.

[e] Goodness of fit.

**Supplementary Table 8 Bader charges analysis of CoMn-MOCs-500 in FFCA oxidation**

| Atom[a] | CoMn-MOCs-500 | R-CHO* | Gem-diol* |
|---|---|---|---|
| Mn | +1.56 | +1.64 | +1.62 |
| $Co_1$ | +1.34 | +1.33 | +1.27 |
| $Co_2$ | +1.29 | +1.38 | +1.15 |
| $Co_3$ | +1.30 | +1.29 | +1.33 |
| $O_1$ | −0.95 | −0.93 | −1.10 |
| $O_2$ | −1.01 | −1.03 | −1.02 |
| $O_3$ | −0.88 | −0.97 | −1.06 |
| $O_4$ | −1.10 | −1.16 | −1.03 |
| $O_5$ | -- | −1.07 | −1.16 |
| C | -- | +0.84 | +0.99 |
| $H_1$ | -- | +0.15 | +0.03 |
| $H_2$ | -- | -- | +0.69 |

[a] Atoms were identified in Supplementary Figure 43.

## References


1. Siankevich, S. et al. A novel platinum nanocatalyst for the oxidation of 5-Hydroxymethylfurfural into 2,5-furandicarboxylic acid under mild conditions. *J. Catal.* **315**, 67–74 (2014).

2. Kresse, G. & Hafner, J. Ab initio molecular-dynamics simulation of the liquid-metal--amorphous-semiconductor transition in germanium. *Phys. Rev. B* **49**, 14251–14269, (1994).

3. Kresse, G. & Joubert, D. From ultrasoft pseudopotentials to the projector augmented-wave method. *Phys. Rev. B* **59**, 1758–1775 (1999).

4. Blöchl, P. E. Projector augmented-wave method. *Phys. Rev. B* **50**, 17953–17979 (1994).

5. Monkhorst, H. J. & Pack, J. D. Special points for Brillouin-zone integrations. *Phys. Rev. B* **13**, 5188–5192 (1976).

6. Henkelman, G., Uberuaga, B. P. & Jónsson, H. A climbing image nudged elastic band method for finding saddle points and minimum energy paths. *J. Chem. Phys.* **113**, 9901–9904 (2000).

7. Zhao, X., Zhang, F., Xu, S., Evans, D. G. & Duan, X. From layered double hydroxides to ZnO-based mixed metal oxides by thermal decomposition: transformation mechanism and UV-blocking properties of the product. *Chem. Mater.* **22**, 3933–3942 (2010).

8. Rong, S., Zhang, P., Liu, F. & Yang, Y. Engineering crystal facet of α-$MnO_2$ nanowire for highly efficient catalytic oxidation of carcinogenic airborne formaldehyde. *ACS Catal.* **8**, 3435–3446 (2018).

9. Bing, W. et al. A CaMnAl-hydrotalcite solid basic catalyst toward the aldol condensation reaction with a comparable level to liquid alkali catalysts. *Green Chem.* **20**, 3071–3080 (2018).

10. Wang, X. et al. Geometrical-site-dependent catalytic activity of ordered mesoporous Co-Based spinel for benzene oxidation: *In situ* DRIFTS study coupled with Raman and XAFS spectroscopy. *ACS Catal.* **7**, 1626–1636 (2017).

11. Song, Y. et al. Ultrathin layered double hydroxides nanosheets array towards efficient electrooxidation of 5-hydroxymethylfurfural coupled with hydrogen generation. *Appl. Catal. B: Environ.* **299**, 120669 (2021).

12. Serrano, A. et al. Complete oxidation of hydroxymethylfurfural to furandicarboxylic acid by

aryl-alcohol oxidase. *Biotechnol. Biofuels* **12**, 217 (2019).

13. Tian, Z. Y., Tchoua Ngamou, P. H., Vannier, V., Kohse-Höinghaus, K. & Bahlawane, N. Catalytic oxidation of VOCs over mixed Co–Mn oxides. *Appl. Catal. B: Environ.* **117**–**118**, 125–134, (2012).

14. Liu, H. et al. Vitamin C-assisted synthesized Mn–Co oxides with improved oxygen vacancy concentration: boosting lattice oxygen activity for the air-oxidation of 5-(hydroxymethyl)furfural. *ACS Catal.* **11**, 7828–7844 (2021).

15. Liu, X., Zhang, M. & Li, Z. $CoO_x$-MC (MC = mesoporous carbon) for highly efficient oxidation of 5-hydroxymethylfurfural (5-HMF) to 2,5-furandicarboxylic acid (FDCA). *ACS Sustain. Chem. Eng.* **8**, 4801–4808 (2020).

16. Bao, L., Sun, F. Z., Zhang, G. Y. & Hu, T. L. Aerobic oxidation of 5-hydroxymethylfurfural to 2,5-furandicarboxylic acid over holey 2D $Mn_2O_3$ nanoflakes from a Mn-based MOF. *ChemSusChem* **13**, 548–555 (2020).

17. Hayashi, E. et al. Effect of $MnO_2$ crystal structure on aerobic oxidation of 5-hydroxymethylfurfural to 2,5-furandicarboxylic acid. *J. Am. Chem. Soc.* **141**, 890–900 (2019).

18. Rao, K. T. V. et al. Inexpensive but highly efficient Co–Mn mixed-oxide catalysts for selective oxidation of 5-hydroxymethylfurfural to 2,5-furandicarboxylic acid. *ChemSusChem* **11**, 3323–3334 (2018).

19. Ventura, M. et al. Tunable mixed oxides based on $CeO_2$ for the selective aerobic oxidation of 5-(hydroxymethyl)furfural to FDCA in water. *Green Chem.* **20**, 3921–3926 (2018).

20. Hayashi, E., Komanoya, T., Kamata, K. & Hara, M. Heterogeneously-catalyzed aerobic oxidation of 5-hydroxymethylfurfural to 2,5-furandicarboxylic acid with $MnO_2$. *ChemSusChem* **10**, 654–658 (2017).

21. Han, X., Li, C., Liu, X., Xia, Q. & Wang, Y. Selective oxidation of 5-hydroxymethylfurfural to 2,5-furandicarboxylic acid over $MnO_x$–$CeO_2$ composite catalysts. *Green Chem.* **19**, 996–1004 (2017).

22. Neațu, F. et al. Selective oxidation of 5-hydroxymethyl furfural over non-precious metal heterogeneous catalysts. *Appl. Catal. B: Environ.* **180**, 751–757 (2016).